1-30-2013

Biological and biomimetic oxygen electro-reduction by enzymes

Shayna Brocato

Shayna Brocato
Candidate

Chemical and Nuclear Engineering
Department

This dissertation is approved, and it is acceptable in quality and form for publication:

Approved by the Dissertation Committee:

Plamen Atanassov, Chairperson

Eva Chi

Scott S. Sibbett

Shelley Minteer

BIOLOGICAL AND BIOMIMETIC OXYGEN ELECTRO-REDUCTION BY ENZYMES

by

SHAYNA BROCATO

B.S. Biochemistry, University of New Mexico, 2008

DISSERTATION

Submitted in Partial Fulfillment of the
Requirements for the Degree of

Doctor of Philosophy
Engineering

The University of New Mexico
Albuquerque, New Mexico

December, 2012

Biological and Biomimetic Oxygen Electro-Reduction by Enzymes

by

Shayna Brocato

B.S. Biochemistry, University of New Mexico, 2008

Ph.D. Engineering, University of New Mexico, 2012

ABSTRACT

Enzyme catalysts are a viable alternative to the traditional platinum based catalysts for the complete oxidation of complex fuels. Efficient oxidation of multi-carbon compounds, selective catalytic activity eliminating the need for fuel purification, and high performance under mild temperature and pH conditions make enzyme catalysts appealing for applications *in vivo*, implantable, and *in vitro*, portable energy sources.

The full catalytic potential of enzymes can only be obtained if the full energy potential of a biofuel, complete oxidation to CO_2, is obtained; this requires multiple reactions, i.e. multiple enzymes or an enzyme cascade. The efficiency of enzyme cascades improves with quaternary protein structures which increase the local substrate concentrations, decrease the distance between enzyme active sites, and limit inhibitory molecules from reaching the active site of the enzymes.

We have established a proof of concept that quaternary protein architectures can be achieved through DNA directed assemblies. The engineered enzyme conjugate of the

small laccase enzyme from *Streptomyces coelicolor* (SLAC) and zinc finger DNA binding domain from Zif268 is demonstrated to bind double stranded DNA in a site specific manner while retaining enzymatic activity. The proof of principle for DNA templated enzyme immobilization demonstrates the feasibility of engineering quaternary protein structures for efficient oxidation of complex biofuels.

Fuel cells most commonly utilize oxygen as the oxidant at the cathode because oxygen is a strong terminal electron acceptor that allows the extraction of large amounts of energy from the fuel with a non-toxic reduction product, H_2O. Due to the chemical inertness of molecular oxygen under ambient conditions, a catalyst is required for its reduction. The oxygen reduction reaction (ORR) has traditionally been catalyzed by platinum group metal catalysts, but due to their limited supply/availability and high cost are gradually being replaced by enzyme and non-platinum group metal (non-PGM) catalysts.

The SLAC enzyme is a member of the large multicopper oxidase (MCO) family of enzymes that perform oxygen reduction and share a similar 4-copper active site. MCO enzymes are commonly used at the cathode of biofuel cells to catalyze oxygen reduction despite the lack of understanding of the oxygen reduction direct electron transfer (DET) mechanism.

The mechanism of oxygen reduction in the MCOs SLAC and bilirubin oxidase (BOD) were investigated using a rotating ring-disc electrode (RRDE). The DET mechanism in BOD was determined to be a four electron mechanism and in SLAC was determined to be a two electron mechanism. The structure-function relationship of the T1 copper active site in SLAC, investigated through mutating amino acid residues around

the T1 site, showed that amino acid mutations T232F and M298F had the greatest detrimental effects and M198L and T232V had the most positive effects on current and half wave potential. The mechanistic analysis of the multicopper oxidases SLAC and BOD will allow for a deeper understanding of the commonly used ORR mechanism in enzymes.

Non-PGM catalysts are developed based on microcycles and have been proposed for biomimetics of hemoglobin and cytochromes, oxygen reduction complexes. These biomimics for electrocatalysis need a cathode that operates at neutral pH, requiring an understanding of the ORR mechanism and necessitating a full pH study.

The activity of the non-PGM catalyst, Fe-phenanthroline, was tested on an RRDE in electrolyte solutions with pHs ranging from 1 to 13.7. The Fe-phenanthroline ORR mechanism is determined to shift at pH 7 from an inner-Helmholtz plane (IHP) reaction in acidic media to a combination of IHP and outer-Helmholtz plane (OHP) reaction mechanisms in alkaline media as determined through the percent hydrogen peroxide detected at the ring, half-wave potential shift, kinetic current changes, and trends in the number of electrons transferred as calculated from Koutecky-Levich and charge/mass balance analysis. The pH study of Fe-phenanthroline provides a deeper understanding of how pH influences the mechanism and kinetics of oxygen reduction in non-PGM catalysts.

Table of Contents

List of Figures

Chapter 1 – Introduction

Respiration can be based on molecular oxygen, nitrogen, fumarate, sulfate, carbon dioxide, etc. as the terminal electron acceptor [1]. Among these bioavailable oxidants, oxygen is the strongest terminal electron acceptor allowing the extraction of the largest amount of energy from the fuel/food, Figure 1.1. The high abundance of molecular oxygen on Earth, its high permeation rate across biological membranes, and the non-toxic reduction product H_2O make oxygen a very useful terminal electron acceptor for aerobic organisms and the cathode of fuel cells [2].

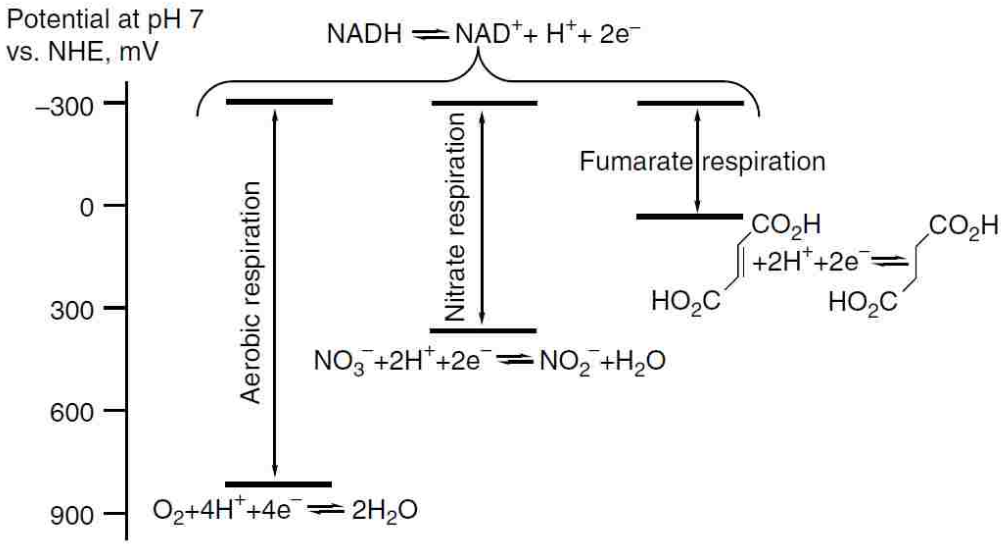

Figure 1.1 – Comparison of the free energy of respiration based on oxygen (anerobic), nitrate, and fumarate [3].

Molecular oxygen is a $4e^-/4H^+$ oxidant that is kinetically inert under ambient conditions, requiring a catalyst for oxygen reduction at rates and electrochemical

potentials that are useful for energy metabolism. Enzymes from the terminal oxidase family of enzymes catalyze the reduction of O_2 to H_2O in aerobic organisms and are present in all three domains of life, Bacteria, Archaea, and Eukarya [4-5]. The oxygen reduction in fuel cells is traditionally catalyzed by platinum based metals, but has recently been catalyzed by non-platinum group metals and enzymes.

1.1 Biofuel cell principles

Biofuel cells are a class of fuel cells that utilize enzymes or bacteria as the catalyst for the oxidation and reduction of biofuels such as ethanol, glucose, and glycerol. The basic operating principle of a biofuel cell is the same as conventional fuel cells. Fuel is oxidized at the anode, releasing electrons and protons. The electrons travel through an external circuit to produce power and the protons travel through a membrane to the cathode where the oxidizing substrate is reduced. Biological fuel cells employ enzymes or microbes as the catalysts at the anode and/or cathode.

1.1.1 Metal vs. enzyme catalysts

Enzymes offer three major advantages over traditional precious metal catalysts for biofuel cells. First, there are numerous enzymes which can catalyze a wide range of reactions with a variety of substrates, whereas metal catalysts are limited in the number of possible substrates/fuels [6-16]. Fuel cells typically utilize precious metals such as platinum to catalyze the oxidation of the fuels to create energy. Precious metals continue as the predominant catalyst because they are better understood and are capable of

efficiently oxidizing simple molecules such as hydrogen, methanol, and formic acid. Metal catalysts are unable, though, to efficiently oxidize compounds that contain more than a single carbon such as ethanol, glucose, ethylene glycol, or glycerol [17-18]. Enzymes have great potential as an alternative to conventional precious metal catalysts because they can efficiently oxidize multi-carbon compounds, termed a complex biofuel. A complex fuel implies a greater energy density of the fuel and higher fuel efficiency, two of the most desired characteristics of fuel cells.

Second, enzymes react selectively with their substrates and are generally not passivated by impurities in the substrate solution, which eliminates the need for substrate/fuel purification [19-20]. Third, unlike precious metal catalyst system, enzymes optimally perform under mild temperature and pH conditions.

1.1.2 Multi-enzyme fuel cells

Increased power and energy are obtained from electrodes in enzymatic biofuel cells with multiple enzymes. This is observed for two reasons: complex fuels can be completely oxidized and there is decreased feedback inhibition. Feedback inhibition refers to a situation where substances at the end of a series of reactions inhibit a reaction at the beginning of the series. Feedback inhibition can be minimized by decreasing the concentration of the inhibitory intermediates by reacting them in a subsequent reaction.

The incorporation of multiple enzymes into fuel cells for the efficient oxidation of biofuels has been demonstrated to increase the power output in both a methanol biofuel cell [11] and a pyruvate/air biofuel cell [21]. The Krebs cycle is the metabolic pathway in eukaryote organisms responsible for completely oxidizing pyruvate to obtain energy for

the cell [22-24]. The Krebs cycle enzymes were incorporated in a pyruvate biofuel cell where it is demonstrated that increasing the number of Krebs cycle enzymes leads to incremental increases in the fuel cell power output with each enzyme added, reaching a maximum when all nine enzymes of the Krebs cycle were incorporated. Figure 1.2 shows representative power curves for the pyruvate/air biofuel cells containing increasing number of Krebs cycle enzymes [21]. The power curves are labels for the number dehydrogenases the biofuel cell contains starting with pyruvate dehydrogenase (1 dehydrogenase), isocitrate dehydrogenase (2 dehydrogenases), α-ketogluterate dehydrogenase (3 dehydrogenases), succinate dehydrogenase (4 dehydrogenases), and malate dehydrogenase containing the complete Krebs cycle (5 dehydrogenases). The biofuel cells, although labeled for the number of dehydrogenase enzyme they contain, incorporate the non-dehydrogenase Krebs cycle enzymes that catalyze the previous Krebs cycle reactions. The observed increases in power output are attributed to the deeper oxidation of the complex biofuel pyruvate.

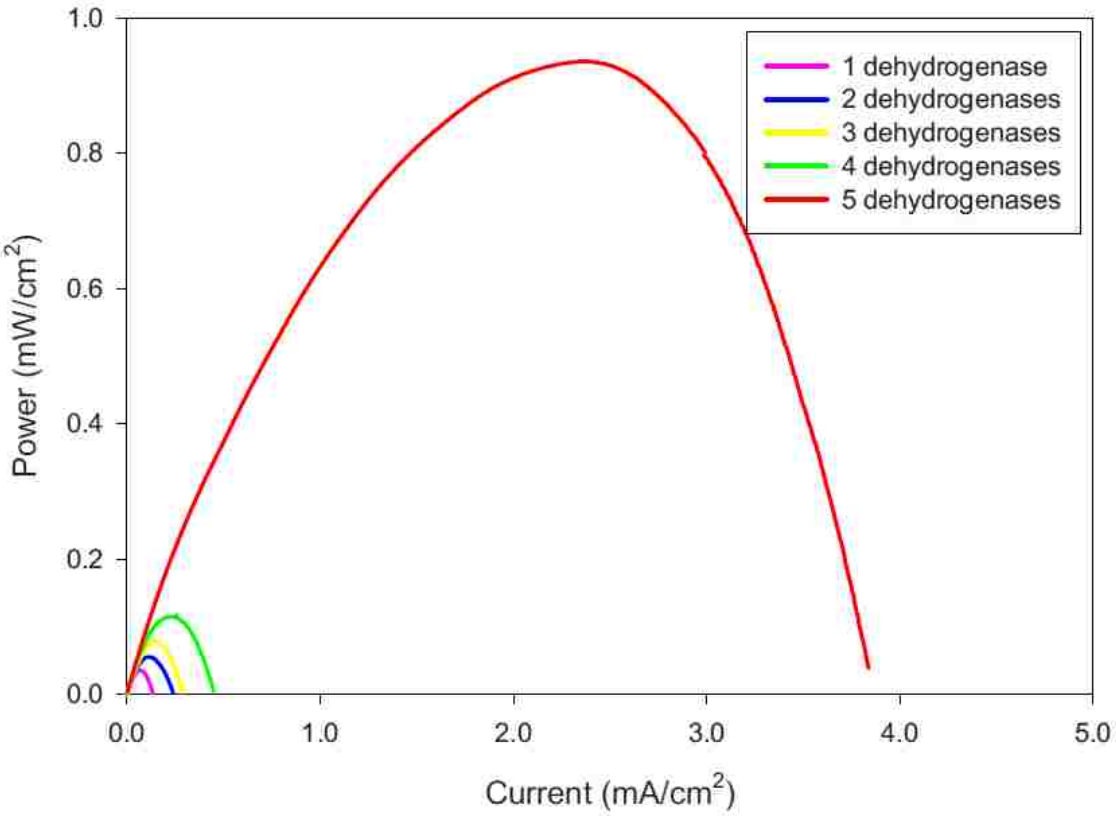

Figure 1.2 – Biofuel cell power output with the enzymes of the Krebs cycle, ending at pyruvate dehydrogenase (1 dehydrogenase), isocitrate dehydrogenase (2 dehydrogenases), α-ketogluterate dehydrogenase (3 dehydrogenases), succinate dehydrogenase (4 dehydrogenases), and malate dehydrogenase containing the complete Krebs cycle (5 dehydrogenases) [21].

1.1.2.1 Substrate specificity

It is often not practical or efficient to incorporate all of the enzymes from a natural metabolic pathway into a fuel cell because it decreases the concentration of each enzyme on the fuel cell electrode, decreasing the current/power obtained. This effect if often minimized through high enzyme loadings on the electrode or by using enzymes that are

engineered or found in nature to have low substrate specificity, i.e. enzymes that are promiscuous. Enzyme promiscuity allows one enzymes to catalyze multiple reactions using different substrates.

In 2009, Arechederra et al. demonstrated that a sequence of three enzymes with low substrate specificity, when combined, is able to completely oxidize glycerol to carbon dioxide [6-8]. The sequence of 3 different enzymes from different organisms performs the same function as the naturally occurring 16 enzyme glycerol oxidation cascade. This glycerol oxidation sequence began with two bacterial enzymes from *Gluconobacter*, pyrroloquinoline quinone-dependent alcohol dehydrogenase (PQQ – ADH) and pyrroloquinoline quinone-dependent aldehyde dehydrogenase (PQQ-AldDH) [25-26]. The natural substrates for PQQ-ADH and PQQ-AldDH are ethanol and acetylaldehyde, respectively, but due to their low substrate specificities these enzymes are able to catalyze reactions with alternative substrates. These two enzymes alone were only able to obtain 70% of the energy that was subsequently achieved after the third enzyme oxalate oxidase was added to the system, Figure 1.3 [6].

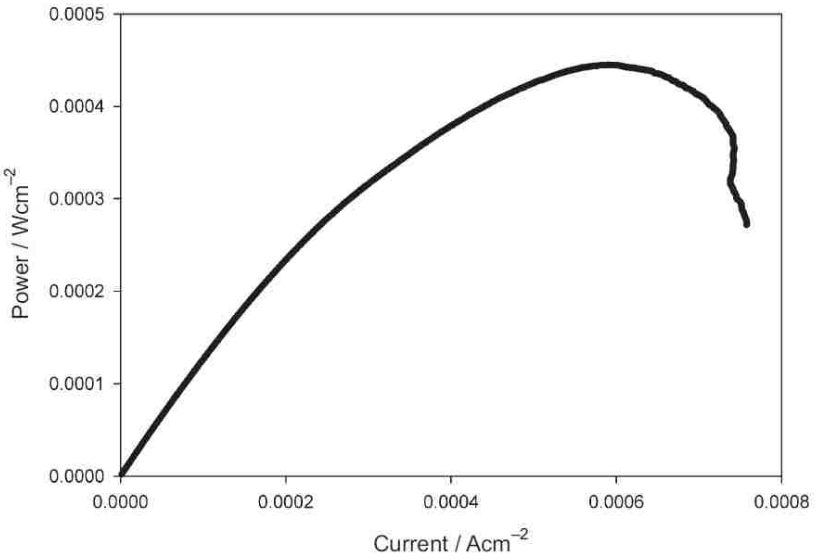

Figure 1.3 – Three enzyme glycerol biofuel cell power curve [6].

In this case, enzymes are preferred over metal catalysts because metal catalysts can only oxidize the first four electrons of the complex fuel glycerol; enzymes can oxidize all 14 of the possible electrons [17]. The complete oxidation of glycerol by enzymes leads to a high fuel cell energy density (energy per unit volume) and the low substrate specificity decreases the number of enzymes required for complete fuel oxidation.

1.1.2.2 Multi-enzyme complex

Multi-enzyme biofuel cells are often diffusion limited, most heavily influenced by the enzymes used, enzyme loading, and environmental conditions such as flow rate, temperature and pH [13]. The multi-enzyme redox systems that are observed in nature have had a lot of time to optimize the conditions for fast mass transport, most of which

we are able to recreate in a lab, but there is one condition that has yet to be mimicked, the multi-enzyme complex termed the metabolon.

1.1.2.2.1 Metabolon

The cell is the basic unit of life. Prokaryotic organisms are distinguished from eukaryotic organisms by the cell compartmentalization. Eukaryotic cells are structurally and functionally compartmentalized into the nucleus, mitochondria, chloroplast, lysosomes, golgi bodies, plasma membrane, cytoskeleton, cell wall, etc. It is hypothesized that the metabolic enzymes within a single compartment are complexed in sequential or at the very least non-random arrangements [24, 27]. Evidence for complexes of sequential metabolic enzymes is present, in varying degrees, for many metabolic pathways of the cell, Table 1 [24]. The observed multi-enzyme complexes have been termed protein machines, clusters, supramolecular complexes, aggregates, hyperstructures, cellulosomes, and metabolons.

Table 1. Evidence for complexes of sequential metabolic enzymes. A – channeling; B – specific protein-protein interactions; C – specific protein membrane interactions; D – kinetic effects; E – isolation of complexes or multi-functional proteins; F – genetic evidence; G – model systems; H – existence of multifunctional or multi-enzymatic proteins; I – physical chemical evidence [24].

Metabolic pathway	Evidence
DNA biosynthesis	A,B,C,E,F*
RNA biosynthesis	A,B,C,E,F
Protein biosynthesis	A,B,C,D,F
Glycogen biosynthesis	B,E
Purine biosynthesis	A,E
Pyrimidine biosynthesis	A,B,D,E,F
Amino acid metabolism	A,B,D,H
Lipid biosynthesis	B,C,F,H
Steroid biosynthesis	A,C,E
Glycolysis	A,B,C,D,E,I
Tricarboxylic acid cycle	B,C,D,G
Fatty acid oxidation	A,B,C,D
Electron transport	C,I
Antibiotic biosynthesis	A,E
Urea cycle	B,D
Cyclic AMP degradation	A,D,E

Cellular compartmentalization and multi-enzyme complexes formed between sequential enzymes in a metabolic pathway are hypothesized to contribute to the efficiencies found in these systems in three major ways [28]. First, enzymatic catalytic efficiency is increased by channeling intermediates formed at the active site of one enzyme to the active site of the subsequent enzyme, illustrated in Figure 1.4. This effectively brings the active sites of the enzymes in a metabolic pathway into close proximity thereby decreasing transit time for the intermediates. Second, kinetic constraints associated with dilute concentrations of intermediates are decreased. Third,

the multi-enzyme structure prevents inhibitory molecules from reaching the active site of the enzyme.

Yunfeng Lu, at the Biomedical Engineering Seminar at UNM, suggested that the efficiency of a two enzyme system can be increased by 500% and a three enzyme system can be increased by 1500% through the formation of metabolon-like structures compared to random immobilization [29], the latter technique previously demonstrated by Moehlenbrock et al., 2010 [30].

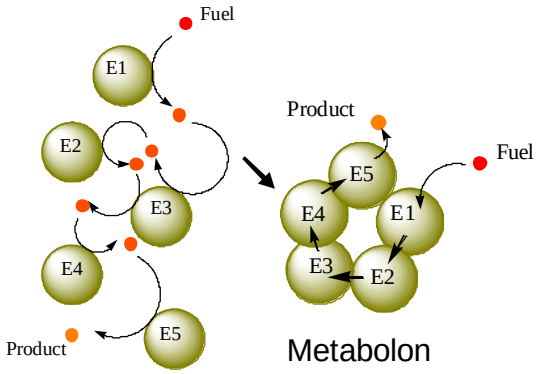

Figure 1.4 - Metabolic pathway of enzymes forms a metabolon structure for greater catalytic efficiency.

The theory that multi-enzyme complexes are needed for the observed cellular efficiency has two major criticisms. First, since substrate diffusion rates are on the order of microseconds while enzyme turnover rates are in the range of milliseconds, such complexes are not necessary. Second, the multi-enzyme complexes that have been demonstrated have only been done so in-vitro. It is these in vitro observations that have been hypothesized to extend to *in vivo* systems. The reported interactions between the

enzymes in multi-enzyme complexes that were isolated from a cell were very weak and often required special conditions to be demonstrated. Volume-excluding molecules (aka osmolytes), such as polyethylene glycol, enhance weak forces that hold together enzymes. This technique for increasing the weak forces is criticized because it does not mimic the *in vivo* cellular conditions, yet the effects on the enzymes has been suggested to extend to the *in vivo* system. Regardless whether multi-enzyme complexes occur *in vivo*, increased enzyme performance has been demonstrated in vitro and this knowledge can be used to engineer more efficient enzymatic for applications include biosensors, bioelectronics, and bioenergy.

1.1.2.2.2 Cross-linked enzymes

The importance of multi-enzyme complexes to the catalytic efficiency of enzymatic systems was demonstrated by Moehlenbrock et al. in 2010 by approximating the naturally observed multi-enzyme complexes through cross-linking the enzymes of the Krebs cycle [30]. Mitochondria were introduced to a cross-linking agent, glutaraldehyde or dimethyl suberimidate for 5 minutes. During this time proteins were nonspecifically linked to other proteins in a close proximity. When the Krebs cycle enzymes were purified from the mitochondria lysate, the Krebs cycle enzymes were cross-linked. The subsequent incorporation into the pyruvate/air biofuel cell saw dramatic increases in both current and power densities compared to the uncomplexed enzymes, Figure 1.5. These results demonstrate the importance of the metabolon structure and enzyme-enzyme proximity for efficient substrate transport between enzymes when engineering multi-enzyme devices.

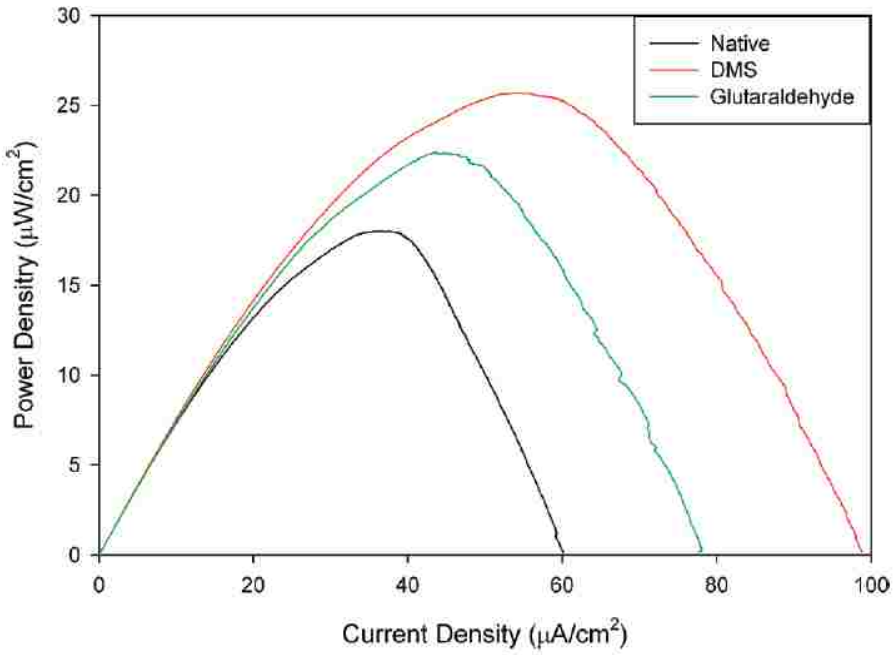

Figure 1.5 - Power curves of un-cross-linked and DMS and glutaraldehyde cross-linked Krebs cycle enzymes from mitochondrial electrodes [30].

The method for cross-linking enzymes presented in the metabolon catalyzed pyruvate/air biofuel cell requires the enzymes to be preassembled into multi-enzyme complexes prior to isolation from the cell or incorporation into an enzymatic device. Ultimately, this method is limited to easily accessible, naturally associating/close proximity enzymes and cannot be extended to engineered enzyme or enzymes selected from different organisms such as the glycerol fuel cell in Arechederra et al., 2009 and the glucose oxidase/peroxidase cascade [6].

The glucose oxidase/peroxidase enzyme cascade is a set of reactions that is used for determining the free glucose in body fluids, food, and agricultural products [31].

Glucose oxidase catalyzes the oxidation of β-D-glucose to D-glucono-δ-lactone while simultaneously reducing oxygen to hydrogen peroxide. Peroxidase then reduces the hydrogen peroxide to water with concomitant oxidation of a color changing substrate whose color development is tracked spectroscopically. Since the glucose oxidase/peroxidase enzyme cascade contains enzymes that come from different organisms, the enzymes could not be effectively cross-linked using DMS or glutaraldehyde to approximate a multi-enzyme complex.

1.2 Biomimetics

Multi-enzyme complexes that are self-assembling could be engineered through maco-molecular templating using biomimetics. Biomimetics is the science of adapting designs from nature to solve modern engineering problems. For example, Velcro was developed by Swiss chemist George de Mestral by copying the way cockleburs clung to his dogs fur [32].

Self assembling, multi-enzyme complexes could be engineered using biomimetics of the cellulosome. The cellulosome is a highly elaborate, cell-bound multi-enzyme complex present in bacteria that breaks down cellulose and hemicellulose. The cellulosome is created through enzymatic domains linked linearly along a scaffold protein through high-affinity ($>10^9$ M^{-1}) cohesion-dockerin interactions, illustrated in Figure 1.6 [33-36].

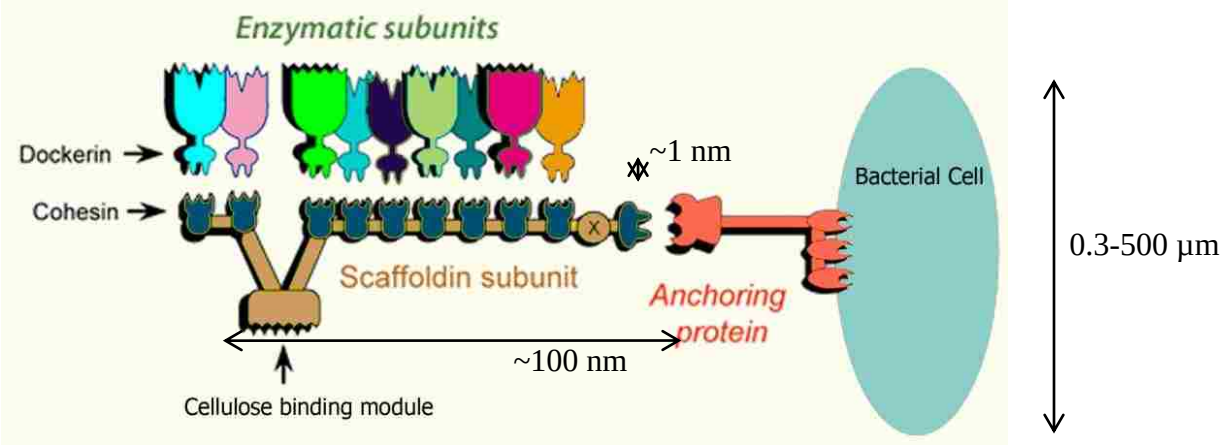

Figure 1.6 - Cellulosome complex [35].

The dockerin and cohesion proteins work together to provide site specific binding along the length of the scaffoldin. The scaffoldin and cohesion proteins provide an angstrom length scale template for protein (dockerin) docking. By mimicking this natural system, site specific enzyme immobilization could be engineered to obtain self-assembling, multi-enzyme complexes.

1.3.1 DNA template for protein binding

DNA could replace the scaffoldin and cohesion proteins for an angstrom length scale template for protein docking. DNA is made of four bases, adenine (A), cytosine (C), thymine (T), and guanine (G), whose sequences create binding sites for molecules involved in DNA transcription and translation. Some of these DNA binding molecules are transcription factors. Transcription factors are proteins that bind to specific DNA sequences through a DNA-binding region of the protein. These DNA binding protein

regions include the helix-turn-helix, helix-loop-helix, leucine zipper, and zinc finger. DNA with its variable nucleic acid sequence can provide a template for transcription factor binding. DNA binding proteins can be localized anywhere along the variable DNA sequence without affecting its biophysical properties, making DNA an excellent biomimetic template, performing the same role as the scaffoldin and cohesion proteins in cellulosomes [37-38].

1.3.2 Zinc fingers for DNA-protein attachment

The dockerin proteins linked to enzymes can be approximated using the DNA binding zinc finger protein domains covalently linked to enzymes, Figure 1.7. Zinc fingers are DNA-binding protein domains observed in numerous transcription factors. The DNA attachment occurs through cysteine and histidine linked to nucleic acids, an angstrom length scale interaction [39].

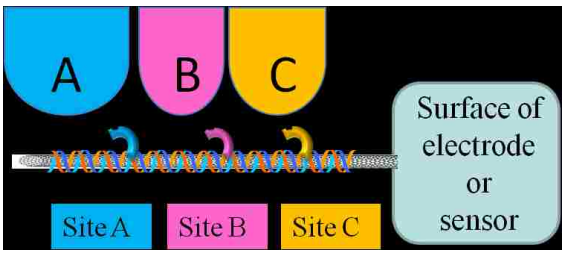

Figure 1.7 – DNA templated protein attachment schematic. Enzymes A, B, and C are conjugated to zinc fingers which are site specifically attaching to a double stranded-DNA wrapped single walled carbon nanotube on the surface of an electrode or sensor.

Each zinc finger recognizes a three nucleic acid sequence and each transcription factor has between 3-12 zinc fingers (depending on the transcription factor) making the DNA recognition site 9-36 nucleic acids or more, Figure 1.8. It is this modular structure and binding specificity of the transcription factor DNA binding domains, such as the zinc finger domain, that allow for the docking in a sequence specific manner, a nanometer length scale effect which propagates to the micrometer length scale [36]. Redox enzymes can be conjugated/attached to the DNA binding domains. This is a general approach that will allow any redox enzyme to be modified and site-specifically immobilized on a DNA strand, allowing the rational assembly of organized multi-enzyme complexes.

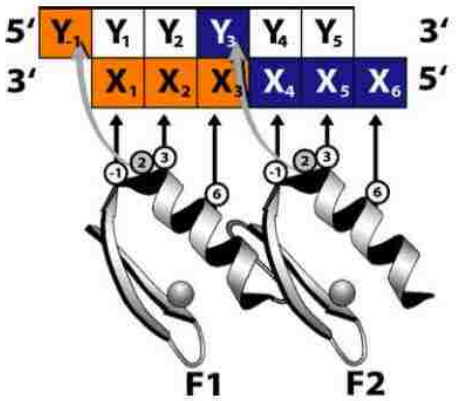

Figure 1.8 – Zinc finger DNA binding motif [40].

1.3 DNA-templated enzymatic biofuel cell applications

Enzymatic biofuel cells have many practical applications in implantable (*in vivo*) devices and portable energy sources (*ex vivo*). The attraction and allure of enzymatic biofuel cells

initially began with *in vivo* applications in mind: pacemakers, glucose sensor for diabetics, small valve for bladder control, etc. Enzymatic biofuel cells are ideal for *in vivo* applications because they utilize *in vivo* fuels and operate at physiological temperature and pH.

The advantages of enzymatic biofuel cells have resulted in increased research efforts to implement enzymes into many applications, especially power sources and sensors [41]. Enzymes are currently being used in *ex vivo*, low temperature biofuel cells and biosensors such as the glycerol biofuel cell [6], laccase-glucose oxidase biofuel cell [42], urea sensor [43] and glucose sensor [44]. Enzymatic biofuel cells are commercially available for limited use, outside the U.S, but generally are in various stages of research and development. Enzyme stability (active lifetime), enzyme orientation for direct electron transfer (DET), and slow substrate diffusion in multi-enzyme pathways currently limit the application for enzymatic biofuel cells [41].

It has been demonstrated that higher current and power output is obtained from biofuel cells that use multiple enzymes compared to a single enzyme and when the enzymes are attached/cross-linked to each other compared to uncross-linked. The method for cross-linking enzymes presented in the metabolon catalyzed pyruvate/air biofuel cell [45] requires the enzymes to be preassembled into multi-enzyme complexes prior to isolation from the cell or incorporation into an enzymatic device. Ultimately, this method of cross-linking to achieve a higher performing biofuel cell is limited to easily accessible, naturally associating/close proximity enzymes and cannot be extended to engineered enzyme or enzymes selected from different organisms such as the glycerol fuel cell [6]. The prospect of developing a method to obtain multi-enzyme complexes that

is not enzyme specific drives the development of self assembling, multi-enzyme complexes through a DNA-templated system.

The DNA-templated system for engineering multi-enzyme complexes would stand apart from other enzymatic biofuel cell systems because it will allow multiple enzymes to be placed in specific pre-determined arrangements on the electrode. These self-assembling, multi-enzyme complexes will create an effect similar to natural metabolons, increased enzymatic efficiency and minimize transport limitations between the active sites of the enzymes. The DNA-templated system is expected to have a wide range of applications in enzymatic biofuel cells such as: glucose fuel cells, glycerol fuel cells, artificial mitochondria, etc.

1.4 Oxygen Reduction Biomimetics

Oxygen is a powerful 4 electron/4 proton oxidant that is chemically inert under ambient conditions, requiring catalysis to achieve a reaction rate useful for energy metabolism. Heme/Cu terminal oxidase enzymes (HCO) catalyze this reduction of oxygen to water; some members of this enzyme family include the cytochrome *c* and quinol oxidases. Biomimetic studies of HCOs have been developed using Fe porphyrins (heme/Cu analogs) in an effort to reproduce the oxygen reactivity observed in enzymes in a synthetic system, design useful synthetic catalysts, and better understand the oxygen reduction mechanism and the structure/activity relationship of an enzymatic catalytic site by studying the biomimetic analog. Fe-phenanthroline is a Fe porphyrin biomimetic analog that can be used to elucidate the oxygen reduction mechanism over the full pH range.

Chapter 2 - Problem Statement and Objectives

The development of enzymatic biofuel cell technology is limited by several factors, a major factor being efficiency. The efficiency could be increased by utilizing multiple enzymes, and further increased by arranging the enzymes in a quaternary protein structure. The existence of quaternary protein structures or multi-enzyme complexes between sequential enzymes of metabolic pathways have been demonstrated to induce substrate channeling that results in increased efficiency by increasing the local substrate concentrations, decreasing the distance between enzyme active sites, and limiting inhibitory molecules from reaching the active site of the enzyme. This investigation supports the development of enzymatic biofuel cells through providing the enabling technologies for developing self-assembling, multi-enzyme complexes. The primary objective of this work is to demonstrate a proof of concept that quaternary protein architectures can be achieved through DNA directed assemblies.

- **Objective 1:** Confirm that the small laccase-zinc finger conjugate enzyme (SLAC-3ZF) retains a high level of catalytic activity in both the DNA bound and un-bound states.

- **Objective 2:** Demonstrate that SLAC-3ZF binds DNA is a sequence specific manner.

The new bi-functional redox protein, the small laccase enzyme (SLAC) that has been appended to a zinc-finger DNA-binding domain, SLAC-3ZF, will be used to

evaluate for activity and DNA-binding capabilities. The SLAC-3ZF kinetics will be determined using an 2,2'-azino-bis(3-ethylbenzothiazoline-6-sulphonic acid) or ABTS spectroscopic assay.

The specificity of the SLAC-3ZF binding to double stranded DNA will be evaluated using surface plasmon resonance and a magnetic bead capture assay. The magnetic bead capture assay which utilizes ABTS as an indicator molecule will also confirm enzyme activity in the DNA bound state.

- **Objective 3:** Identify which amino acid residues around the T1 copper center in SLAC affect the intramolecular charge transfer and how they affect the overall catalysis.

The catalytic mechanism of the small laccase has not been well documented or studied. To gain a better understanding of our SLAC-3ZF conjugate and the SLAC enzyme, a mechanistic study on the DET of the oxygen reduction reaction will be performed on the wild type-SLAC and SLAC with mutations around the T1 copper center. The amino-acids around the T1 copper center are believed to influence the intermolecular electron transfer. These SLAC mutants and SLAC-wild type will be evaluated electrochemically by linear scan voltammetry using a rotating ring-disc electrode (RRDE) setup to determine effect of the point mutations on the oxygen reduction catalysis.

- **Objective 4:** Elucidate the DET ORR mechanism of bilirubin oxidase using a RRDE setup.

The SLAC enzyme is just one member of the very large family of multi-copper oxidase enzymes which share similar copper active sites. There is little knowledge on the mechanism of oxygen reduction occurring in any of the multi-copper oxidase enzymes. A mechanistic study on the multi-copper oxidase enzyme bilirubin oxidase will be performed using a RRDE setup.

- **Objective 5:** Elucidate the ORR mechanisms over the full pH range and determine if/where the oxygen reduction mechanism shifts as a function of pH.

The ORR mechanism may shift as a function of the pH of the electrolyte solution. There is very little data on the ORR mechanism in neutral media, necessary for the incorporation of enzymes into fuel cells. To eliminate possible variability in observed activity/current etc. consistent with enzymes, the ORR mechanism will be investigated using a Fe-N-C containing catalyst named Fe-phenanthroline. The ORR mechanism on Fe-phenanthroline will be analyzed over the full pH range from pH 1 to pH 14 using electrochemical measurements carried out on a RRDE setup.

Chapter 3 – Experimental Methods

3.1 Surface plasmon resonance (SPR)

SPR is a technique is commonly used for investigating protein binding: affinity and kinetics. It is an optical technique that utilizes the resonance of a surface plasmon wave with the incident light wave to detect small mass changes on a surface, Figure 3.1. Monochromatic light is passed through a prism and onto a glass surface coated with 20-50 nm thick noble metal that has a full d-subshell, i.e. silver, gold or copper. The light is then reflected or partially transmitted through the metal layer. The incidence angle that leads to the lowest reflected light intensity is the surface plasmon resonance angle (Θ_{SPR}). If the wave vector of the incident light matches the wavelength of the surface plasmons, free oscillating electrons at the surface of the metal layer, resonate creating an evanescent wave that extends approximately 200-300nm from the metal surface into the sample medium, Figure 3.1. It is this area where mass changes can be detected. The resonance frequency of the SPR wave (and thus the Θ_{SPR}) depends on the refractive index of the sample medium (*n*). The SPR instrument uses a photo-detector array to measure minute changes in Θ_{SPR}.

The SPR is advantageous over techniques such as quartz crystal microbalance and fluorescent molecular tagging because it does not require any labels, provides reproducible data, is very sensitive (only >50 pg/mm^2 of analyte is needed for detection), binding events are observed in real-time with a rapid response, and can measures the control surface (no protein binding) simultaneously. The change in Θ_{SPR} of 10^{-4} degrees is approximately equal to 1 µg of protein/mm^2.

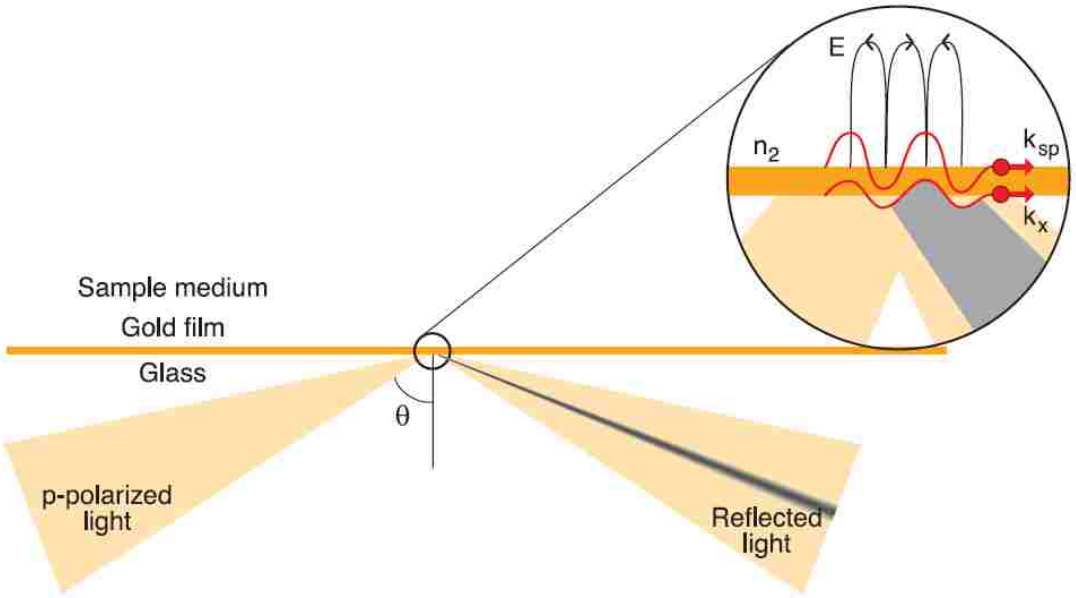

Figure 3.1 – SPR schematic [46]. The surface plasmon wave (k_{sp}) is excited by the x-component of the incident p-polarized light (k_x) at a glass/metal interface enhancing the evanescent field (E) amplitude.

3.1.1 Detecting Protein-DNA binding using surface plasmon resonance

In this work, protein binding to DNA was analyzed using SPR with a DNA coated gold chip. Prior to surface modification, gold chips (50 nm thick gold with a 2 nm thick chromium underlayer purchased from Biosensing Instrument, Tempe, AZ) were cleaned with a 3:1 piranha solution, sulfuric acid: hydrogen peroxide (from chemical sources with analytical purity that were used as received), for 5 minutes and then washed thoroughly with water treated with a Millipore Milli-Q water purification system. After cleaning, physical adsorption was used to coat the gold chips with DNA. The 47 base DNA oligos

(sequence shown below) purchased from Integrated DNA Technologies (IA) contain two Zif-268 zinc finger binding sites (underlined).

Sense 5'- TAC CAT GGA GCG TGG GCG TAT GAA TTC TAG CGT GGG CGT AAG CTT AT-3'

Antisense 5'- ATA AGC TTA CGC CCA CGC TAG AAT TCA TAC GCC CAC GCT CCA TGG TA -3

Sense and antisense strands were annealed at 95° C for 10 minutes and then allowed to cool to room temperature. The gold chips were soaked in 20 μM annealed DNA overnight. The gold chip was then washed with DI water followed by ethanol, DI water, and then dried with nitrogen gas.

The DNA coated gold chips were confirmed to be fully coated with DNA using SPR. Cysteine, a small thiol containing amino acid known to bind gold through gold-thiolate bonds, was used to detect uncoated gold surfaces [47]. Injection of 1 mg/ml cysteine (Sigma-Aldrich, St. Louis) resulted in an immediate and significant increase in SPR signal for clean gold chips which remained high for uncoated gold chips and returned to initial levels for DNA coated gold chips indicating that physical DNA adsorption successfully coated the gold chip in DNA.

The SPR measurements were conducted on a BI-SPR 2000 Instrument (Biosensing Instrument Inc., Tempe, Arizona) equipped with a dual-channel flow cell and two through-the-handle six-port injection valves. SPR conditions were the following:

flow rate was 20 µl/min, room temperature, and 80 µl injection volume. Flow buffer was 0.05 M Tris-hydrochloride (EMD Chemicals, Taiwan), 0.5 M Sodium chloride (Mallinckrodt, Inc., St. Louis, MO), and 0.05% IGEPAL CA-630 (Sigma, St. Louis, MO) at pH 6. SLAC-His and SLAC-3ZF-His proteins at 20 µM, diluted in flow buffer, were injected into the SPR. Figure 3.2 illustrates the SLAC-3ZF-His conjugate protein binding to a DNA coated gold sensor surface.

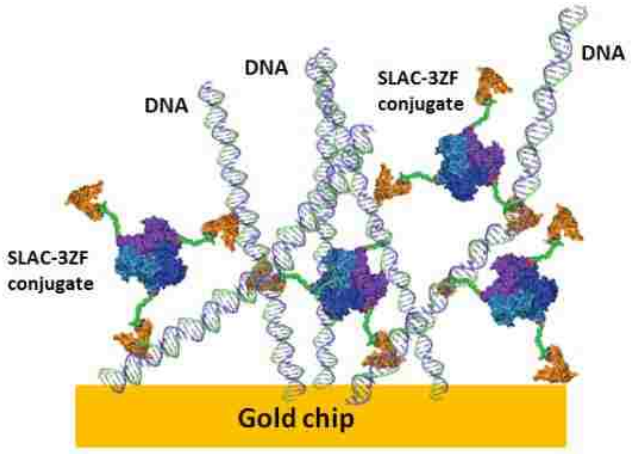

Figure 3.2 - Illustration of nanostructure DNA-SLAC-3ZF complex formation on gold sensor surface in SPR.

3.2 Characterization of catalytic activities

In spectrophotometric assays, the course of a reaction is measured by how much light the assay solution absorbs. If the light absorbed by the assay is within the visible spectrum, 390 nm to 750 nm, then this assay is called a colorimetric assay.

3.2.1 ABTS Colorimetric Assay

ABTS (2,2'-Azinobis [3-ethylbenzothiazoline-6-sulfonic acid]-diammonium salt) is a substrate used for detecting enzyme activity. This substrate changes from colorless to green upon oxidation, Figure 3.3, and the product can be read spectrophotometrically at 405 nm.

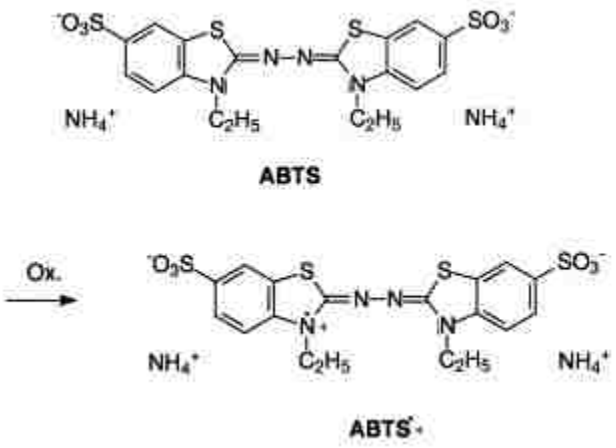

Figure 3.3 –Structure of ABTS, [top] colorless reduced and [bottom] green oxidized.

SLAC-His and SLAC-3ZF-His enzyme kinetics against 0 – 35 mM ABTS (Sigma, St. Louis, MO) were studied at 24.5 nM protein concentration in air-saturated 50 mM sodium acetate buffer, pH 5.0. Oxidation of ABTS was followed at 420 nm, ε = 36,000/(Mcm).

3.2.2 DMP

DMP (2,6-dimethoxyphenol) is a widely used substrate of laccases for determining the kinetics, Figure 3.4. Upon oxidation DMP takes on a bluish-green color which can be read spectrophotometrically at 468 nm.

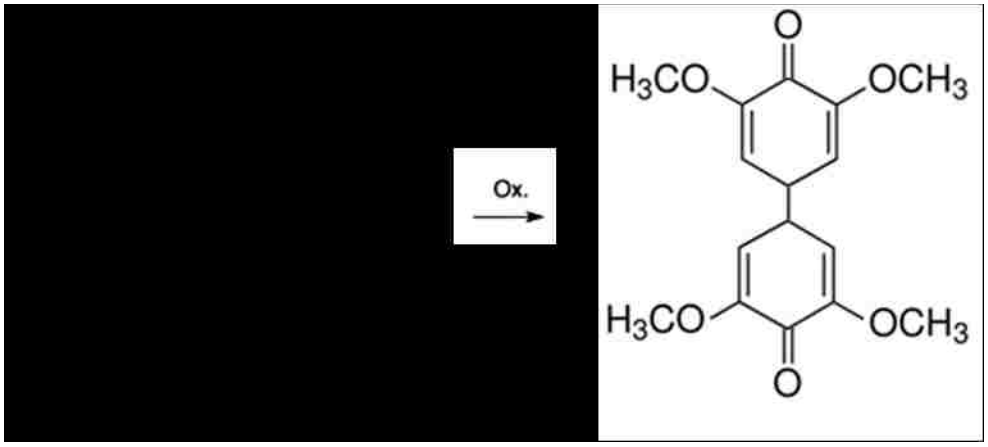

Figure 3.4 –Structure of DMP, [left] colorless reduced and [right] bluish-green oxidized.

SLAC-His and SLAC-3ZF-His enzyme kinetics against 0 – 35 mM DMP (Sigma, St. Louis, MO) were studied at 24.5 nM protein concentration in air-saturated 10 mM sodium phosphate buffer, pH 7.3. Oxidation of DMP was followed at 468 nm, ε = 14,800/(Mcm).

3.3 Detecting DNA binding using a magnetic bead capture assay (MBCA)

The MBCA is a type of colorimetric assay that is used to simultaneously detect molecular binding and enzymatic activity. This research used MBCA to detect the small laccase-zinc finger conjugate enzyme (SLAC-3ZF-His) binding to DNA and confirm enzyme activity during the DNA-bound state. Figure 3.5 illustrates the various steps in the MBCA. Streptavidin coated magnetic beads were washed and re-suspended in assay buffer (10 mM Tris-HCl, 500 mM NaCl, 0.05% (w/v) IGEPAL (Sigma, St. Louis, MO), 1 mM dithiothreitol, 0.1mM ZnSO4 at pH 8), reacted with biotinylated double-stranded DNA (dsDNA) having the nucleotide sequence Biotin-5'-TAT GGA TCC TAC CAT GGA GCG TGG GCG TAA GCT TAT-3' (zinc finger binding sequence underlined) for at least 1 h at 4^{o}C, followed by washing with assay buffer. Control beads were reacted with biotinylated decoy DNA with the sequence Biotin-5'-TAT GGA TCC TAC CAT GGA CCT ATG TGC TAA GCT TAT-3' (no zinc finger binding site) [48].

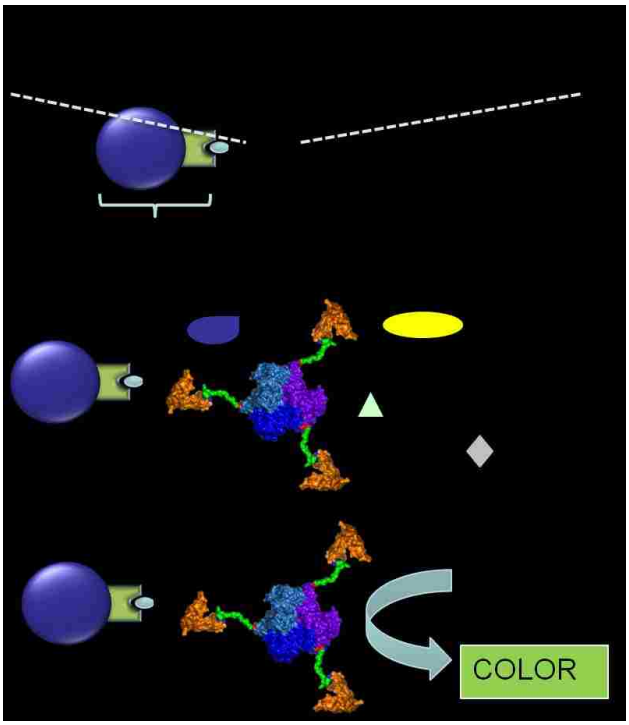

Figure 3.5 – Schematic of the magnetic bead capture assay.

SLAC-His or SLAC-3ZF-His protein was added in assay buffer and incubated with the dsDNA decorated magnetic beads for 1 h after which the beads were excessively washed. The bound enzyme activity was determined by re-suspending the beads in a solution containing 20 mM ABTS and 50 mM sodium-acetate buffer, pH 5.0 and the absorbance read at 420 nm using a SpectraMax M2 (Molecular Devices, Sunnyvale, CA) spectrophotometer. The amount of bound protein was determined from the enzymatic activity of samples and from protein standards. The supplier of the magnetic beads reports that the DNA binding capacity of the beads is 500 pmol/mg of beads. This value was used to calculate the fraction of bound protein per available DNA binding site.

3.4 Electrochemical characterization techniques

All electrochemical experiments were performed with a three-electrode half-cell setup consisting of a working electrode, counter electrode, and a reference electrode. The working electrode is where the catalyst of interest is deposited and is typically made of gold or glassy carbon. The counter electrode passes all the current needed to balance the reaction occurring at the working electrode. The counter electrode must have higher surface area than the working electrode so as not to limit the reaction occurring at the ring electrode and must have electrochemical properties that do not influence the working electrode. The reference electrode is a stable standard which the potential at the working electrode is measured against and is typically made of platinum. No current is passed through the reference electrode.

3.4.1 Cyclic voltammetry

Cyclic voltammetry is a primary technique used for electrochemical characterization to determine the behavior of electrochemical redox reactions. It consists of applying a potential that varies with time to the working electrode using a triangular waveform, Figure 3.6, and measuring the resulting current.

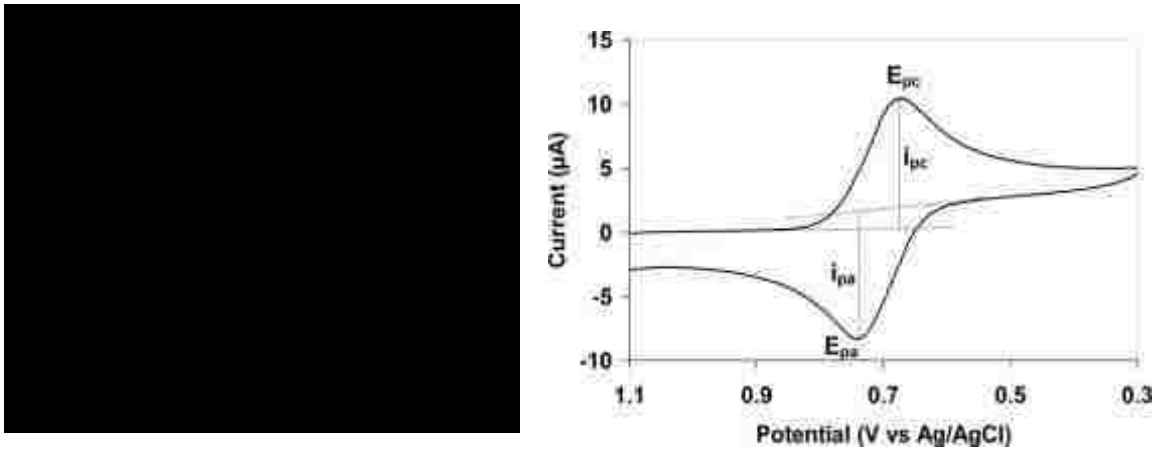

Figure 3.6 – [left] Triangular waveform of a single sweep of a cyclic voltammogram. [right] The resulting, typical cyclic voltammogram.

3.4.1.1 Calculating the electrochemically accessible surface area (ECSA)

The extent of electrochemical accessibility determines the practical utilization of the high surface area MWNT modified glassy carbon electrode. The electrochemically accessible surface area (ECSA) is determined using the following two equations:

$$\boldsymbol{ECSA = \frac{C}{C_{sp}}} \quad \textbf{(1)}$$

$$\boldsymbol{C = \frac{\left(\frac{i}{2}\right)}{scan\ rate}} \quad \textbf{(2)}$$

where C is the capacitance, C_{sp} is the specific capacitance, i is the difference in the anodic and cathodic current at a chosen potential, and the scan rate is in V/s. A cyclic

voltammogram taken under N_2 saturated conditions is used to calculate the ECSA. The absolute magnitude of the anodic and cathodic current taken in a region where no faradic processes are occurring is taken as i. The specific capacitance for carbonaceous MWNT material has a large discrepancy in the literature and ranges from 5 $\mu F/cm^2$ to 80 $\mu F/cm^2$ due to differences in their microtextures and composition [49]; in this work the specific capacitance is taken to be 25 $\mu F/cm^2$.

3.4.2 Linear sweep voltammetry (LSV)

LSV is an alternative voltammetric technique to cyclic voltammetry where the potential is swept linearly in time, in a single direction. This technique is often preferred over cyclic voltammetry for:

1. Unstable enzyme catalysts, such as small laccase or mutant enzymes, because it decreases the potentials swept by 50% which helps to preserve the catalyst kinetics.
2. Quickly measuring the electrochemical reduction or oxidation reaction of irreversible reactions which only occur either on the anodic or cathodic sweep.

3.4.2.1 Calculating the oxygen reduction reaction (ORR) current

In this work enzyme activity is quantified through the observed ORR current from LSVs. The electrochemical current (Δi) is taken as the difference in current at the onset of oxygen reduction and the steady state current.

3.4.2.2 Calculating the enzyme orientation efficiency

Proper enzyme orientation is crucial for DET to occur [50]. The orientation efficiency is the amount of enzyme on the electrode interface that can perform direct electron transfer as determined through the electrochemical current observed. No signal will be detected from the enzymes that are not properly oriented for DET, unless a mediator is present. Orientation efficiency is calculated using the following equation:

$$Orientation\ Efficiency = \frac{60000\Delta i}{LUnN_A e^-} * 100\% \quad (3)$$

where Δi is the change in the oxygen reduction current measured, L is the catalyst loading (0.1 mg), U is the specific activity of the enzyme in U/mg, n is the number of electrons transferred per mole of substrate (4 e^-), N_A is Avogadro's number (6.0221415×10^{23}/mol), and e^- is the charge of an electron (1.607×10^{-19} C).

3.4.3 Rotating ring-disc electrode (RRDE)

A RRDE is an electrode containing two working electrodes, a disc and a ring, which are used to simultaneously characterize two electrochemical reactions. The RRDE is rotated with an angular velocity (ω) which creates a fluid flow profile that draws solution up towards the disc and out parallel to the disc surface, Figure 3.7. Rotating the electrode increases the substrate concentration at the electrode surface, thereby, eliminating mass transfer effects and allowing researchers to isolate and study reaction kinetics.

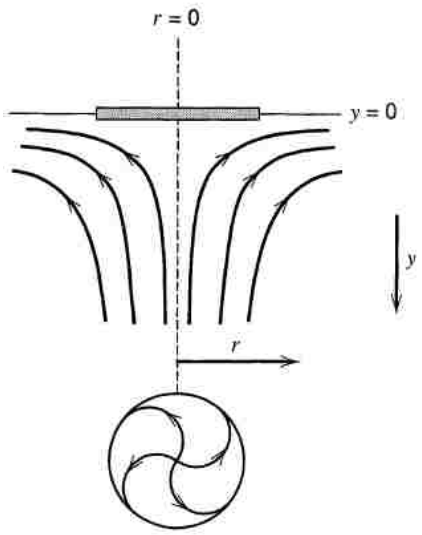

Figure 3.7 – Fluid flow profile underneath the RRDE, [top] side view and [bottom] bottom up view [51].

This research used a thin gap RRDE containing an inert glassy carbon disc and a Pt ring, a WEB30 Pine bi-potentiostat, and a Pine Instruments Rotator (Pine Instruments, Durham, NC), Figure 3.8, to investigate the oxygen reduction reaction in small laccase, bilirubin oxidase, and Fe-phenanthroline. The catalyst of interest was immobilized on the disc and the was potential was swept to obtain CVs or LSVs. Simultaneously, the Pt ring was polarized between 0.6V and 1.1V, depending on the pH of the electrochemical solution, to detect hydrogen peroxide coming from the ORR occurring on the disc.

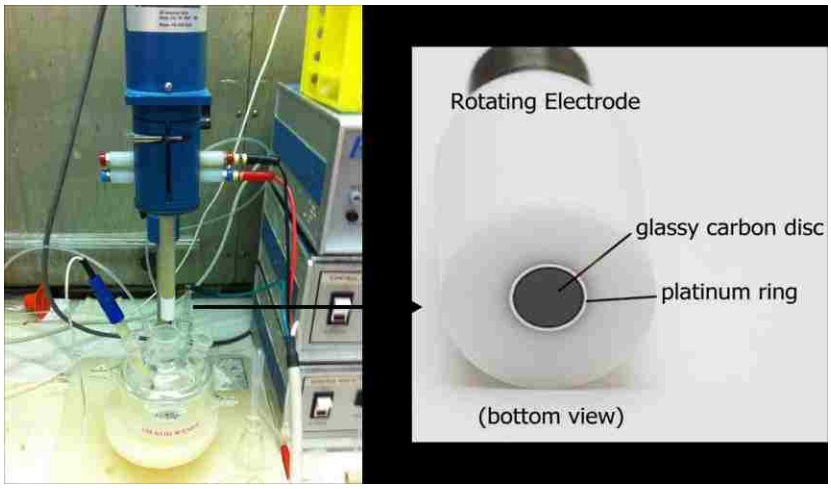

Figure 3.8 – [left] RRDE setup and [right] Pine thin gap RRDE.

3.4.3.1 Calculating the percent hydrogen peroxide (H_2O_2)

The percent of H_2O_2 generated from the disc in a RRDE can be estimated using the following equation:

$$\%\boldsymbol{H_2O_2} = \mathbf{100} * \left[\frac{\mathbf{2}\boldsymbol{I_R}}{\boldsymbol{NI_D} + \boldsymbol{I_R}}\right] \quad \textbf{(4)}$$

where I_R and I_D are the currents observed at the ring and disc, respectively, and N is the collection efficiency of the RRDE (N = 0.37) [52-53].

3.4.3.2 RRDE analysis methods

The RRDE disc and ring currents obtained from systems under kinetic control (not mass transfer limited) can be analyzed using the charge/mass balance and Koutecky-Levich

analysis methods to elucidate reaction parameters such as the number of electrons transferred and the kinetic rate constant of the electrochemical rate limiting step.

3.4.3.2.1 Charge/mass balance

The average number of electrons transferred per oxygen molecule can be calculated from the 2 and 4 electron mass and charge balances given by the equation:

$$\boldsymbol{n = \frac{4}{1+\frac{i_R}{\eta i_D}}} \quad \textbf{(5)}$$

where n is the number of electrons transferred, i_R is the ring current, η is the collection efficiency (η = 37%), and i_D is the disc current [52, 54-56].

3.4.3.2.1 Koutecky-Levich analysis

According to the Koutecky-Levich theory, the disc current (i_d) on a rotating disc electrode can be described using equation:

$$\boldsymbol{\frac{1}{i_d} = \frac{1}{i_k} + \frac{1}{i_L} = \frac{1}{i_k} + \frac{1}{(0.62)nFAD^{\frac{2}{3}}\nu^{\frac{-1}{6}}C\omega^{\frac{1}{2}}} = \frac{1}{i_k} + \frac{1}{B\omega^{\frac{1}{2}}}} \quad \textbf{(6)}$$

where i_k is the kinetic current density of the ORR (an electrode dependent parameter), i_L is the mass transfer limited current, n is the number of electrons transferred per oxygen molecule, Faraday's constant (F) is 96485 C/mol, area (A) of the RRDE disc is 0.2472

cm^2, diffusion coefficient of oxygen (D) is 2.6 x 10^{-5} cm^2/s, kinematic viscosity (ν) is 0.009 cm^2/s, the solubility of oxygen (C) is 1.26 x 10^{-6} mol/cm^3, and ω is the RRDE angular rotation rate in rads/s [51, 57]. According to equation 6, the plot of the inverse current as a function of the inverse square root of the angular velocity can give the kinetic current density (calculated from the y-intercept) and the overall electron transfer number (calculated from the slope, 1/B, given the by the strait line equations) if the values of C and *v* are known.

The kinetic rate constant (k) is given by

$$\boldsymbol{k = \frac{i_k}{nFAC}} \quad \textbf{(7)}$$

where the kinetic current (i_k) is given by the y-intercept ($1/i_k$) in the Koutecky-Levich plot, n is the number of electrons transferred per oxygen molecule, Faraday's constant (F) is 96485 C/mol, area (A) of the disc of the RRDE is 0.2472 cm^2, and the solubility of oxygen (C) is 1.26 x 10^{-6} mol/cm^3 [51-52].

The fundamental limitations of the Koutecky-Levich equation restrict its use to systems under complete kinetic control. Thick, porous catalyst layers do not provide free diffusion at the disc surface making them unsuitable to Koutecky-Levich analysis ultimately limiting its use to ultra thin, uniform catalyst layers where diffusion at the electrode surface is not constrained.

3.5 Scanning Electron Microscopy (SEM)

SEM is a technique that provides information on nano-scale surface morphology. An electron beam at accelerating voltages from 2-30 keV is used to probe a sample surface under vacuum conditions. The depth of the sample probed is controlled by varying the accelerating voltage of the electron beam. The electrons from the electron beam interact with the sample where they lose energy through surface collisions and are scattered off the sample surface at angles different from the electron beam and detected by the SEM or absorbed by the sample surface. The beam current that is absorbed by the sample surface is used to create images of the sample. In this work SEM was used to image MWNT and Fe-phenanthroline surfaces.

3.6 Expressing and purifying SLAC and SLAC-3ZF

The small laccase enzyme (SLAC) is not available commercially but has been expressed and purified from Escherichia coli (E.coli) cells. In this work E.coli BL21(DE3) cells (Invitrogen, CA) that had been transvected with the SLAC-His and SLAC-3ZF-His vectors (generous gift from the Scott Banta group, Columbia University, NY) were grown for protein expression.

Bacterial colonies were grown on a lysogeny broth (LB) media-agarose plate with ampicillin. LB is a nutritionally rich medium used for the growth of E.coli bacteria and the antibiotic ampicillin is used to select for cultures containing successfully transvected cells which contain the vector coding for SLAC and ampicillin resistance. The protein expression cells were grown in Terrific Broth media at 30^{o}C while shaking until OD_{600}

was approximately 1.5. The temperature was then reduced to 25^{o}C and expression was induced with 0.4 mM isopropyl β-D-1-thiogalactopyranoside (IPTG, Sigma, St. Louis, MO). The lowered temperature is believed to slow down the protein synthesis, allowing time for proper protein folding. The IPTG induces expression of the *lac* operon in E.coli by binding to the *lac1* repressor and altering its conformation preventing the repression of *lacZ*, the β-galactosidase coding gene. All steps are done in autoclaved media.

After 20 h of expression, the cells were collected by centrifugation at 5,000 x g for 10 min at 4^{o}C. Cell pellets corresponding to 0.5 L cultures were re-suspended in 50 mL binding buffer (50 mM tris, 20 mM imidazole, 500 mM NaCl at pH 8.0) supplemented with 0.1 mM phenylmethylsulphonyl fluoride and EDTA-free protease inhibitor cocktail tablet (Roche, Indianapolis, IN), and subsequently sonicated using a microtip probe to lyse the cells. The insoluble material was removed by centrifugation at 24,000 x g for 30 min at 4^{o}C. The resulting soluble fraction was supplemented with 1 mM $CuSO_4$ and 1 mM $ZnSO_4$ and incubated in a rotator at 4^{o}C.

SLAC-His and SLAC-3ZF-His were purified from the soluble fraction by immobilized metal ion affinity chromatography using a 5 mL HisTrap FF crude column (GE Healthcare Life Sciences, Pittsburgh, PA) that had been equilibrated with binding buffer. Bound proteins were eluted with binding buffer containing 260 mM imidazole. Fractions containing SLAC-His or SLAC-3ZF-His, blue in color, were pooled, imidazole concentration was lowered to approximately 0.01 mM, and the protein was concentrated by ultrafiltration (EMD Millipore, Billerica, MA). The protein purity was determined using SDS-PAGE, Figure 3.9. SLAC protein concentrations were determined by absorbance at 590 nm, $\varepsilon = 4400/(Mcm)$ [58].

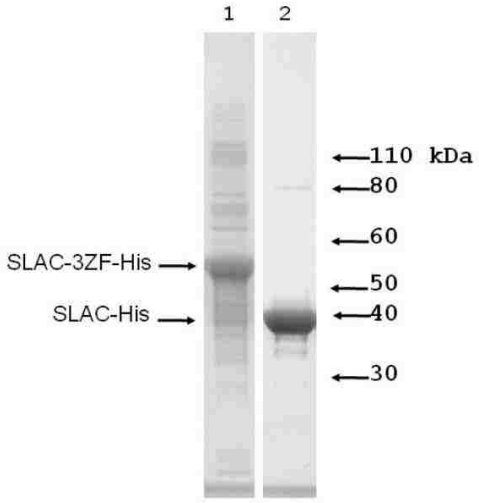

Figure 3.9 – SDS-PAGE of purified SLAC-3ZF-His (1) and SLAC-His (2). Molecular weight standards are indicated.

3.6.1 Sodium dodecyl sulfate polyacrylamide gel electrophoresis (SDS-PAGE)

SDS-PAGE is a technique used for protein separation based on electrophoretic mobility and is useful for determining protein purity. The protein sample to be analyzed is mixed with a 0.1% sodium dodecyl sulfate (SDS) solution. SDS is an anionic detergent which denatures secondary and non-disulfide-linked tertiary structures, essentially linearizing and applying a negative charge to each protein.

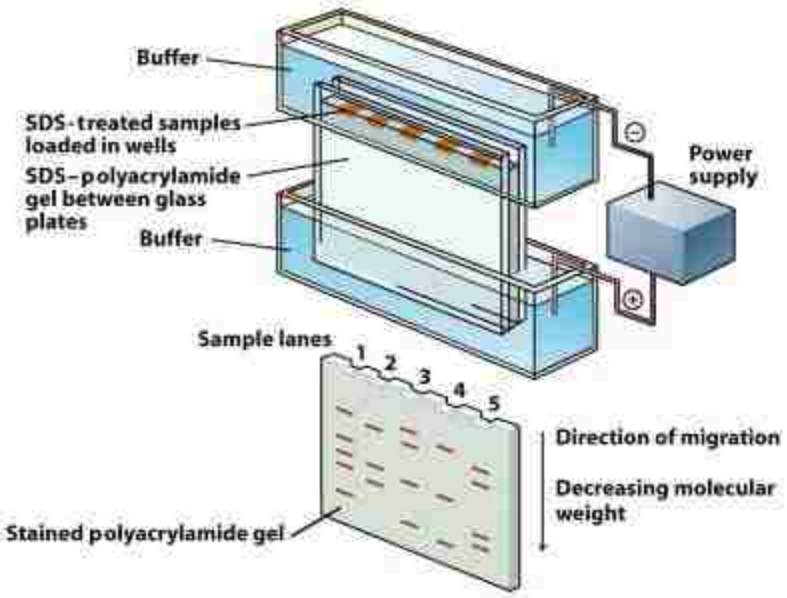

Figure 3.10 – SDS-PAGE schematic [59].

A SDS-polyacrylamide gel is placed in electrophoresis buffer. The SDS treated protein sample or a protein ladder and a bromophenol blue tracking dye is placed in each well of the polyacrylamide gel. The tracking dye is a small molecule with high electrophoretic mobility that is used to visualize the front of the protein solution traveling through the gel during electrophoresis. The protein ladder is a commercial solution of known proteins with a range of molecular weights used to determine the molecular weight of proteins within the sample. A current of 10 mA is applied to the gel causing the negatively charged proteins to travel through the gel towards the cathode. Differences in protein electrophoretic mobility through the porous polyacrylamide gel leads to the proteins moving through the gel at different speeds, separating the various proteins. Once the tracking dye reaches the end of the gel the current is turned off. The proteins are fixed

within the gel and visualized by staining the gel with Coomassie blue allowing researchers to determine the protein concentration and purity by analyzing the color and size of each blue band in the gel.

Chapter 4 – Engineering of a redox protein for DNA-directed assembly

4.1 Introduction

Multi-enzyme pathways play a central role in energy conversion in living cells, primarily in respiration and photosynthesis [34, 60]. The efficiencies found in these systems partially arise from biomolecular self-assembly of the component enzymes in an effort to avoid transport limitations. There has been an increasing interest in the engineering of biomimetic systems for applications including biosensors, bioelectronics, and bioenergy. In order to mimic the efficiencies observed in the native systems, new synthetic biology approaches for introducing self-assembly and macromolecular templating will be required. It has been previously demonstrated that redox enzymes can be engineered to be bi-functional so that they self-assemble into amorphous bioactive hydrogels [61-64]. As multiple enzymes are incorporated into these systems, new methods for templating the arrangements of the enzymes will be required such as DNA directed assemblies [37-38].

This research presents a collaborative effort to address this issue by engineering and characterizing a new bi-functional redox protein. We have appended a zinc-finger DNA-binding domain to the small laccase (SLAC) enzyme from Streptomyces coelicolor [58]. The specificity of the zinc finger domain allows for the docking of the active redox enzyme on DNA molecules in a sequence specific manner. This is a general approach that will allow any redox enzyme to be modified and site-specifically immobilized on a DNA strand, allowing the rational assembly of organized multi-enzyme complexes.

The trimeric SLAC enzyme has been genetically fused with a three zinc finger module from a mouse transcription factor Zif268, which specifically binds double-

stranded DNA having the sequence 5'-GCGTGGGCG-3', resulting in the chimeric SLAC–3ZF–His, Figure 4.1 [58, 60, 65]. The SLAC enzyme was chosen for this proof-of-concept due to its high catalytic activity at pH 7, the same specificity for oxygen as other laccases, the same lack of specificity to the reducing substrate, and our previous experience in engineering it for self-assembly [58, 64, 66-68]. Here we examine the assembly of the SLAC–3ZF–His DNA complex using surface plasmon resonance (SPR) and a magnetic bead capture assay (MBCA).

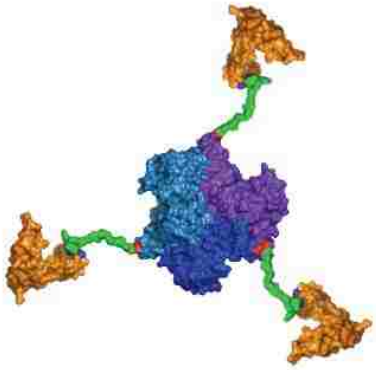

Figure 4.1 - Schematic representation of the multifunctional engineered SLAC–zinc finger fusion protein. The C-terminus of each polypeptide chain in the SLAC trimer (blue, bluish gray, purple) is fused to DNA binding zinc finger domains (brown) via a flexible peptide linker (green). The catalytic sites of the SLAC enzyme are positioned at the subunit interfaces and thus the trimeric structure of SLAC is needed for enzymatic activity. The DNA binding domain is a three zinc finger module from a mouse transcription factor Zif268 that specifically binds double-stranded DNA having the sequence 5'- GCGTGGGCG-3'. The zinc finger structure (brown) is shown in the DNA binding conformation [60].

4.2 Results and Discussion

4.2.1 Characterizing SLAC-His and SLAC-3ZF catalytic activities

The catalytic properties of the fusion protein SLAC–3ZF–His and a control protein SLAC–His were determined for the substrates DMP, Table 4.1, and ABTS, Table 4.2. The Michaelis constants, Km, for SLAC–3ZF–His and SLAC– His fusions were very similar with both DMP and ABTS. The turnover number, kcat, was higher for SLAC–3ZF–His than for SLAC–His using both substrates, but the turnover numbers were lower than what has been reported for the wild type enzyme [58]. Polypeptide fusions added to the C-terminus of the SLAC protein can have a dramatic effect on the catalytic activity of the enzyme, and in previous work the addition of a C-terminal fusion to the SLAC enzyme resulted in a reduction of kcat by two orders of magnitude [64]. In the present work, the impact of the fusions on the activity was far less dramatic.

Table 4.1 - Comparison of SLAC-3ZF-His and SLAC-His enzymatic properties against DMP.

		DMP at pH 7.2		
Protein	Reference	K_M/mM	k_{cat}/min^{-1}	k_{cat}/K_M/M^{-1} min^{-1}
SLAC–3ZF–His	This study	11.7 ± 0.7	172.8	14.8×10^3
SLAC–His	This study	13.0 ± 4.7	55.7	4.27×10^3
HS–SLAC	Wheeldon (2008)	4.2 ± 0.5	2.0	0.48×10^3
SLAC	Machczynski (2004)[10]	~4	~350	$\sim 90 \times 10^3$

Table 4.2 - Comparison of SLAC-3ZF-His and SLAC-His enzymatic properties against ABTS.

		ABTS at pH 5		
Protein	Reference	K_M/mM	k_{cat}/min^{-1}	k_{cat}/K_M/M^{-1} min^{-1}
SLAC–3ZF–His	This study	12.8 ± 1.5	1090.6	85.0×10^3
SLAC–His	This study	13.3 ± 3.0	557.2	41.8×10^3

4.2.2 Detecting protein-DNA binding using SPR

The capability of SLAC–3ZF–His to bind to DNA was tested using surface plasmon resonance (SPR), Figure 4.2. The shift in the SPR signal shows that SLAC–3ZF–His binds to the DNA coated sensor surface, while SLAC–His does not (Fig. 2A). The shift in the SPR signal is proportional to mass changes on the sensor surface, 100 mDeg is approximately proportional to 1 ng/mm^2 of protein [69]. Using this relation, 2.42 ng of SLAC–3ZF–His bound to the surface and 0 ng of SLAC–His. The results show that SLAC–3ZF–His binds the target DNA.

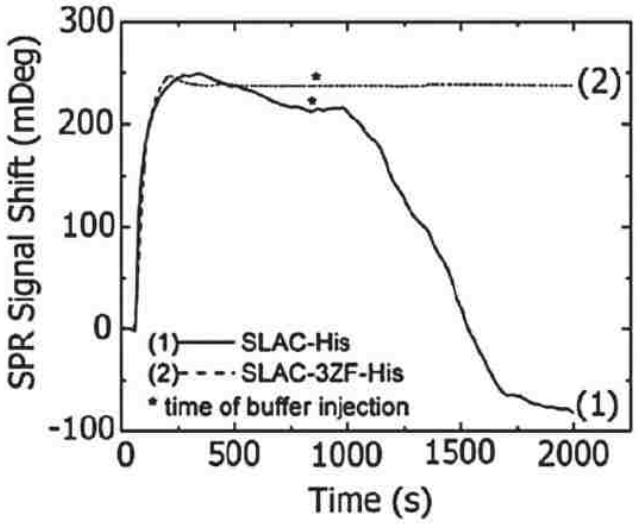

Figure 4.2 – SPR signal shift associated with SLAC-His (1) and SLAC-3ZF-His (2). SLAC–3ZF–His binds to the DNA coated sensor surface and is not washed away. The control protein SLAC–His binds to the surface but is easily washed off.

4.2.3 Detecting DNA binding using a MBCA

The capability of SLAC–3ZF–His to specifically bind to the target DNA sequence was tested using a MBCA. The binding isotherm for SLAC–3ZF–His shows that the fusion protein was able to bind the target DNA on the surface of the magnetic bead, Figure 4.3. The molar amount of bound protein approached the calculated maximum of DNA binding sites on the beads, 65% bound enzyme of available binding sites at 2.75 µM SLAC-3ZF-His. SLAC–3ZF–His binding to the unrelated decoy DNA was very low showing that the DNA binding is sequence specific, 4% bound enzyme of available binding sites at 2.75 µM SLAC-3ZF-His [65, 70]. Non-specific binding to the beads was equally low as well as the binding of the control protein SLAC–His to the target DNA on

the bead surface, 8%, 7%, and 8% bound enzyme of available binding sites at 2.75 μM SLAC-3ZF-His/SLAC-His, respectively. Taken together, the results show that SLAC–3ZF–His specifically and efficiently binds its target DNA on the surface of the magnetic bead and, moreover, is catalytically active in the bound state.

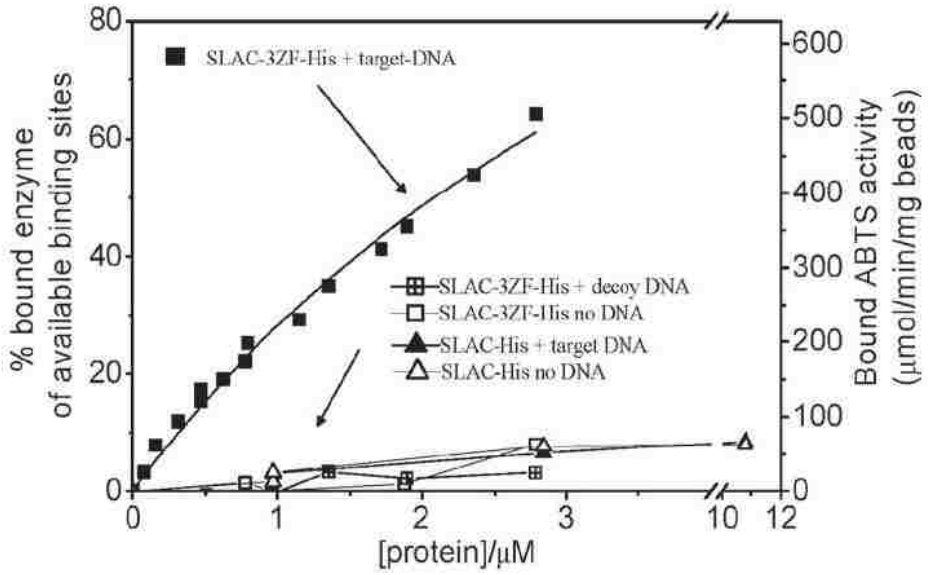

Figure 4.3 - SLAC–3ZF–His and SLAC–His binding isotherms on DNA decorated magnetic beads as assayed by the magnetic bead capture assay. SLAC–3ZF–His bound to the target DNA (filled squares) but not to the decoy (random sequence) DNA (open squares with line) or the beads alone (open squares). The control protein SLAC–His did not bind to the target DNA (filled triangles) or the beads alone (open triangles). The enzymatic activity of SLAC-3ZF-His bound to the beads is shown on the right y-axis. The amount of bound protein was determined from enzymatic activity bound to the beads as described in Section 3.3 - Detecting DNA binding using a magnetic bead capture assay.

4.3 Conclusions

The results from this study show that genetically fusing a DNA binding domain to a laccase enzyme rendered the resulting SLAC–3ZF–His protein bi-functional. We have demonstrated using a magnetic bead assay and SPR that this genetically engineered protein binds to DNA in a sequence specific manner. Furthermore, we have shown that the enzyme retains a high level of activity, even in the DNA-bound state. Thus, DNA strands can be used as templates for enzyme assembly.

Nature uses self-assembly of enzymes to improve catalytic efficiency through the channeling of substrates and increasing the local concentrations of active sites. For example, cellulosome complexes are created by linking enzymatic domains linearly along a scaffold protein using cohesion and dockerin domains [34]. In this work we have demonstrated a similar concept. DNA is an excellent choice for a scaffolding biomolecule since the zinc finger binding sites can be localized anywhere along the DNA sequence without affecting its biophysical properties. This will generate tremendous flexibility in the immobilization of different catalytic domains along the templating scaffold and demonstrate that DNA can act as a template for enzyme immobilization. This research provides the enabling technologies for developing self-assembling, multi-enzyme complexes for electrochemical use. This research is published in Chemical Communications, 2011:

Chapter 4 – Engineering of a redox protein for DNA-directed assembly

Szilvay, G. R., S. Brocato, D. Ivnitski, C. Li, P. D. Iglesia, C. Lau, E. Chi, M. Werner-Washburne, S. Banta, and P. Atanassov (2011). "Engineering of a redox protein for DNA-directed assembly." Chemical Communications **47**(26): 7464-7466.

Chapter 5 – Small laccase mutant study

5.1 Introduction

The small laccase enzyme (SLAC) is a member of the multi-copper oxidase family of enzymes. Members of this family of enzymes share a similar four copper active site and have a broad range of applications from synthesis of heteropolymeric adhesives, preparation of polymeric complexes, production of new antibiotics, and enzymatic delignification [71]. However, the utilization and incorporation of MCOs for stable and efficient biocathodes for these applications still presents barriers, particularly the direct electron transfer between the active site and the cathode surface [72-73]. The turnover rate in MCOs is limited by the electron transfer between the surface and the T1 copper site [74]. This research investigates amino acid mutations around the T1 site to improve the interfacial DET and intramolecular electron transfer from the T1 to T2/T3 trinuclear cluster. The amino acid mutations to be experimentally tested were selected based on a combination of density functional theory, computationally intensive quantum mechanics, and molecular dynamic simulations [75].

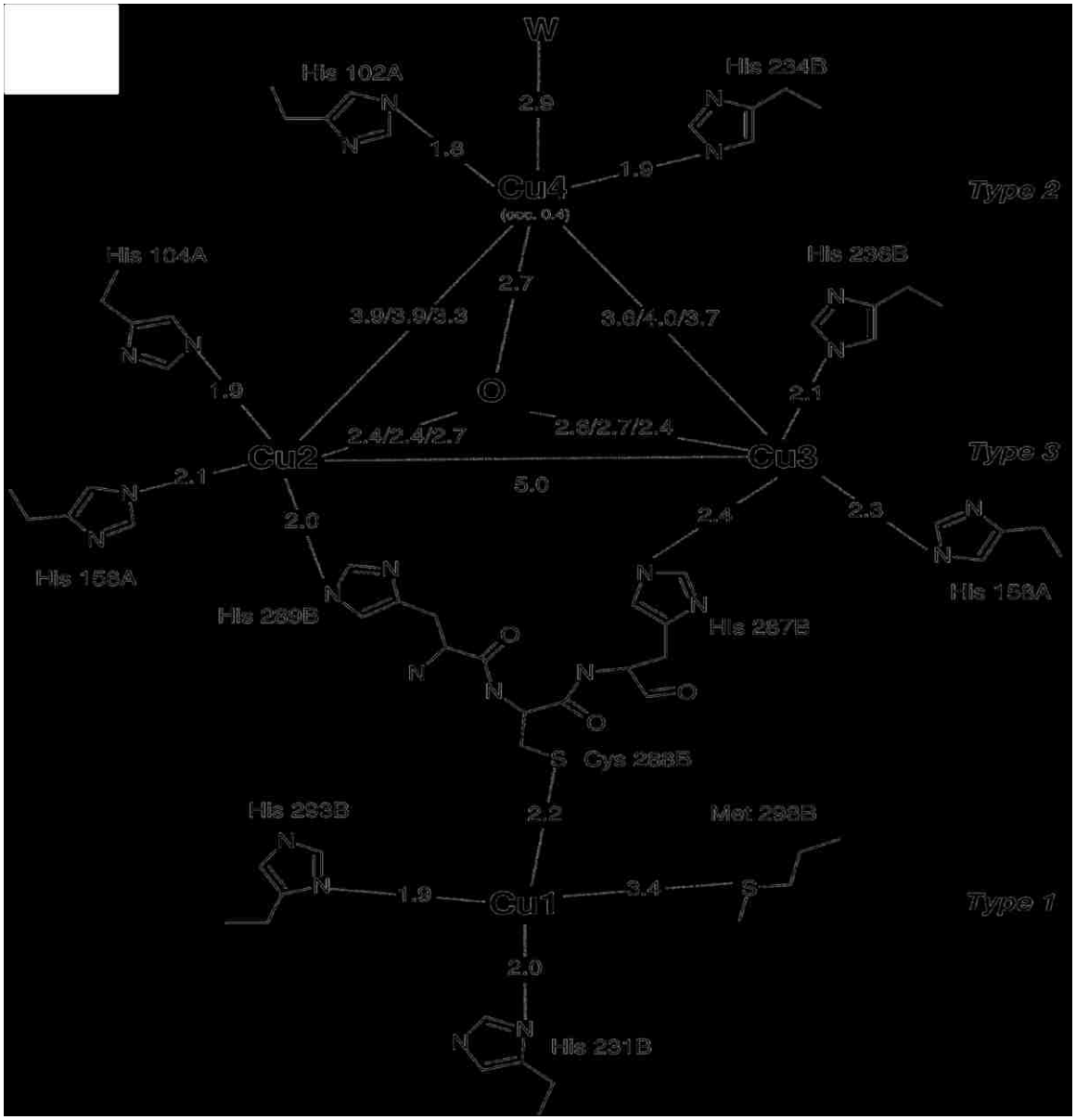

Figure 5.1 – Multi-copper oxidase active site [76].

In this research the oxidation mechanism occurring at the T1 active site is investigated using SLAC enzyme mutants with mutations in the amino acids surrounding the T1 copper site. The SLAC T1 copper and the relative locations of the surrounding amino acids are presented in Figure 5.2. The SLAC mutants were experimentally tested

for open circuit voltage and oxygen reduction reaction (ORR) onset potential using rotating ring-disc electrode (RRDE) electrochemistry.

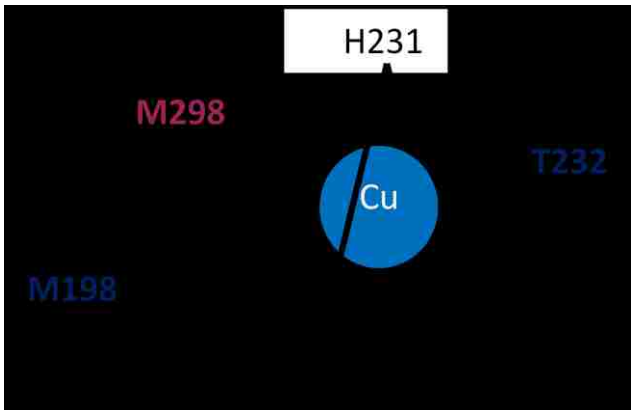

Figure 5.2 – Relative locations of the amino acids surrounding the T1 copper site.

5.2 Experimental

5.2.1 SLAC mutants

The SLAC mutants were obtained from the Airforce Research Laboratories at Tyndall Airforce Base in Panama City, FL. The SLAC enzyme variants tested include:

$SLAC_{WT}$ – wild type enzyme, mutation is a histidine tag for purification purposes and is common among all the mutants

T232F – single mutation, the threonine amino acid at position 232 is mutated to phenylalanine

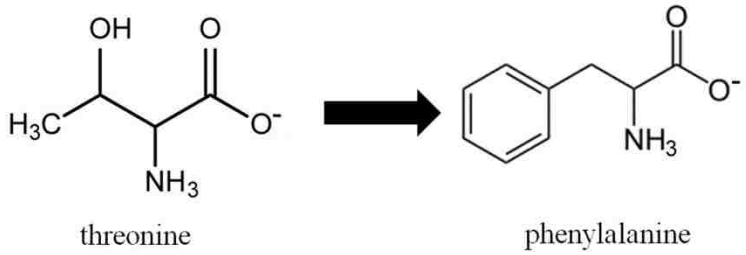

Figure 5.3 – Threonine to phenylalanine mutation.

T232V – single mutation, the threonine amino acid at position 232 is mutated to valine

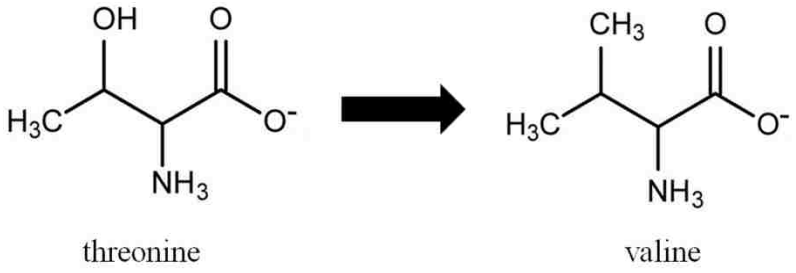

Figure 5.4 – Threonine to valine mutation.

M198L – single mutation, the methionine amino acid at position 198 is mutated to leucine

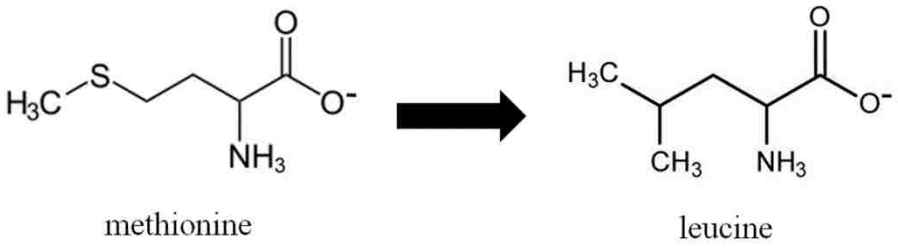

Figure 5.5 – Methionine to leucine mutation.

M298F – single mutation, the methionine amino acid at position 298 is mutated to phenylalanine

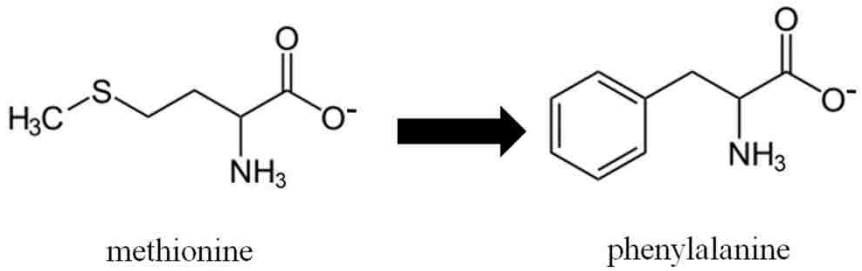

Figure 5.6 – Methionine to phenylalanine mutation.

M198L-T232F – double mutation, the methionine amino acid at position 198 is mutated to leucine and the threonine amino acid at position 232 is mutated to phenylalanine

M198L-T232V – double mutation, the methionine amino acid at position 198 is mutated to leucine and the threonine amino acid at position 232 is mutated to valine

5.2.2 SLAC mutant immobilization procedure

The RRDE was cleaned with alumina, 1 µm, 0.3 µm, followed by 0.05 µm grit with a washing of water in between each grit. A suspension of 5% multi-walled carbon nanotube (MWNT, obtained from cheaptubes.com) in 4:1 water: ethanol (reagent grade, Sigma, St. Louis, MO) and 1% tetrabutylammonium bromide (TBAB) modified Nafion™ polymer

(TBAB-Nafion, a gift from the laboratory of Prof. Shelley Minteer, St. Louis University, MO) were bath sonicated for 30 minutes. The MWNT/TBAB-Nafion suspension was then dropcast on the glassy carbon disc at a loading of 2 mg/cm^2 and dried under nitrogen gas. The enzyme was then dropcast on top of the MWNT/TBAB-Nafion layer and dried under nitrogen gas.

5.2.3 RRDE electrochemical parameters

Electrochemical measurements were performed using a three electrode setup in 0.1 M potassium phosphate buffer, pH 7. The working electrode was the RRDE with the SLAC mutants immobilized, the reference electrode was Ag/AgCl, and the counter electrode was a platinum wire. The disc potential was swept linearly from 0.6 V to 0 V at a scan rate of 10 mV/s while the ring was polarized at 0.8 V. The ring polarization potential of 0.8 V was chosen because it is just below the potential where water begins to split, determined experimentally for the buffer used. Electrochemical measurements were taken under oxygen saturated conditions with the gas bubbling through the cell at room temperature. RRDE rotation rates tested include 1600, 1200, 900, and 400 rpm.

5.3 Results and Discussion

5.3.1 Kinetics of the SLAC mutants

The enzyme kinetics for the SLAC mutants is investigated using a RRDE. The glassy carbon disc of the RRDE contains the dropcast SLAC enzyme (either WT or mutant) on a MWNT/TBAB-Nafion polymer layer. The ORR onset potential is observed to shift in the

mutants from the WT, Figure 5.7 (data shown for 1600 rpm, oxygen saturated conditions). The mutants tested exhibited much lower ORR currents than the $SLAC_{WT}$ but the half-wave potential ($E_{1/2}$) of mutants T232V (p= 0.7) and M198L-T232V (p= 0.8) was observed to increase up to 68 mV from the $SLAC_{WT}$. $E_{1/2}$ was determined using the second derivative. M298L did not have ORR activity. The percent hydrogen peroxide detected on the ring is less than 50% for all mutants and there is no statistical significance between the mutants and WT, Figure 5.8.

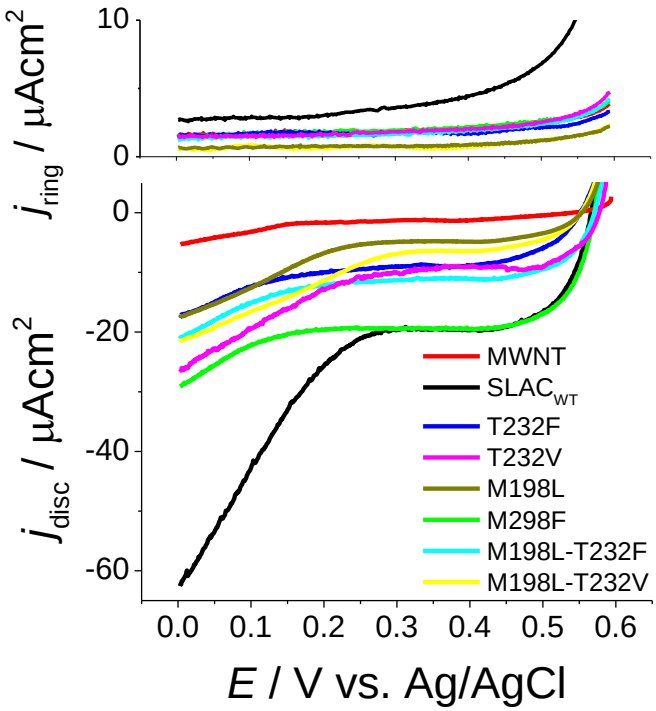

Figure 5.7 - [bottom] RRDE linear scan voltammetry from 0.6 V to 0 V and [top] a plot of the corresponding ring current, polarized at 0.8 V versus the disc potential at 1600 rpm rotation rate under oxygen saturated conditions.

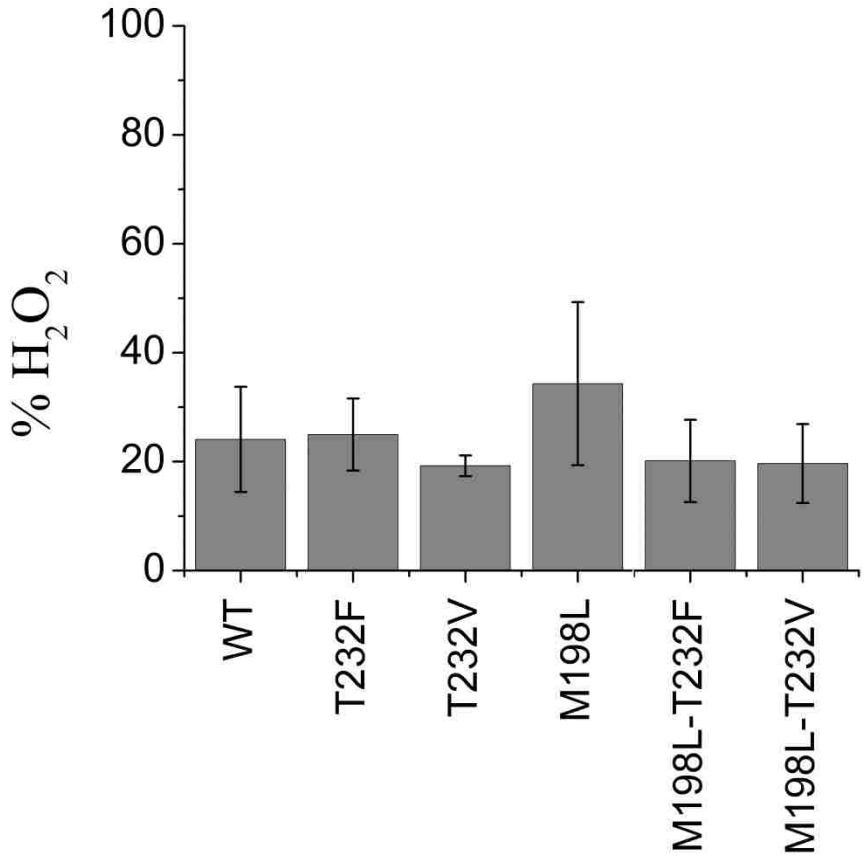

Figure 5.8 – Hydrogen peroxide generated from each mutant.

RRDE data from mutant M198L-T232V, Figure 5.9, is representative of all the mutants and demonstrates how the reductive currents were not significantly different between 400 and 1600 rpms for any of the mutants, indicating very slow enzyme kinetics, and therefore, could not be analyze with Koutecky-Levich or charge/mass balance methods. The results obtained for all the mutants tested in the RRDE experiments are summarized in Table 5.1.

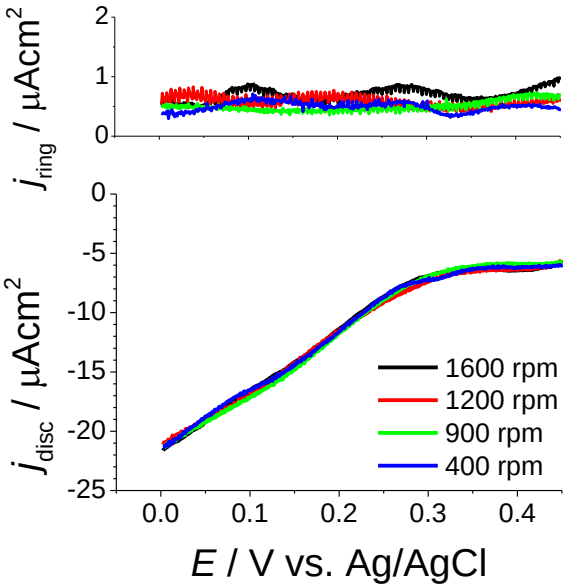

Figure 5.9 – Mutant M198L-T232V RRDE results. [bottom] RRDE linear scan voltammetry from 0.6 V to 0 V and [top] a plot of the corresponding ring current, polarized at 0.8 V versus the disc potential at 1600, 1200, 900, and 400 rpm rotation rates under oxygen saturated conditions.

Table 5.1 – RRDE results summary, p-values vs. WT.

Mutation	$\Delta I_{0.35V-0V}$ / uA mg^{-1}	$E_{1/2}$ / mV
MWTN (control)	0	N/A
WT	-1.80 ± 0.56	98 ± 17
T232F	-0.54 ± 0.14, p = 0.02	61 ± 4, p = 0.02
T232V	-0.61 ± 0.23, p = 0.03	94 ± 4, p = 0.7
M198L	-0.47 ± 0.04, p = 0.01	117 ± 24, p = 0.3
M198L-T232F	-0.57 ± 0.07, p = 0.02	41 ± 1, p = 0.004
M198L-T232V	-0.42 ± 0.08, p = 0.01	109 ± 64, p = 0.8

5.3.2 DET mechanism in SLAC using RRDE

The $SLAC_{WT}$ was kinetically active enough to analyzing using the Koutecky-Levich and charge/mass balance approaches, Figure 5.10. According to the Koutecky-Levich analysis, the number of electrons transferred per molecule of oxygen (n) is 1.9 e^- and the kinetic rate constant (k) is 9.14 x 10^{-5} cm/s. The charge/mass balance calculates n to be slightly greater, varying with potential from 2.5 to 3.5 e^-, Figure 5.11.

The results from the Koutecky-Levich and charge/mass balance analysis, when taken together, indicate that a two electron transfer process is taking place but much of

the hydrogen peroxide generate on the disc is not being detected on the ring. It is likely that the hydrogen peroxide is not being detected by the ring because the catalyst layer is thick and porous, trapping the hydrogen peroxide on the disc. The fundamental limitations of the charge/mass balance equation restricts its use to low porosity systems where intermediates such as hydrogen peroxide are not retained on the disc.

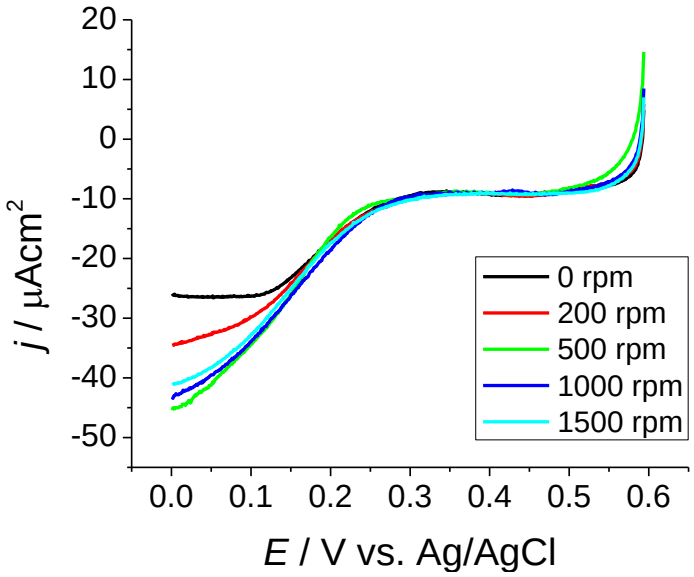

Figure 5.10 – $SLAC_{WT}$ RRDE results. [bottom] RRDE linear scan voltammetry from 0.6 V to 0 V and [top] a plot of the corresponding ring current, polarized at 0.8 V versus the disc potential at 1600, 1200, 900, and 400 rpm rotation rates under oxygen saturated conditions.

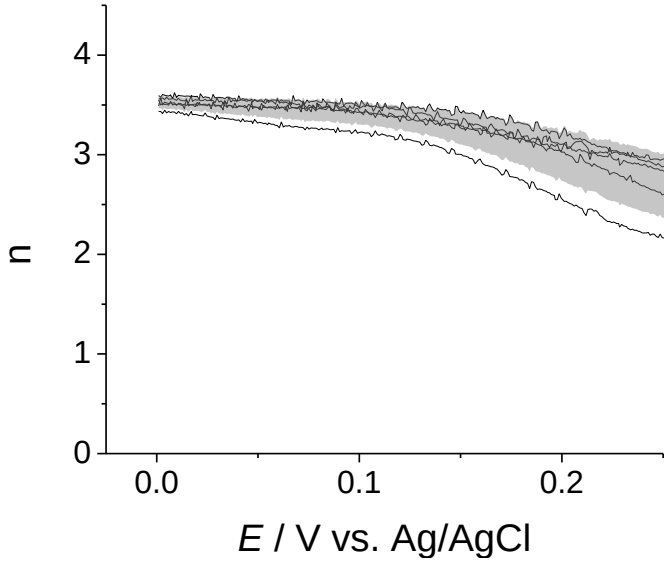

Figure 5.11 – The number of electrons transferred per molecule of oxygen as calculated using the charge/mass balance for a two and four electron transfer mechanism.

5.4 Conclusion

This research aims to understand the structure-function relationship of the MCO T1 copper active site to aid future design of engineered MCOs for efficient biofuel cells. As part of a collaborative effort, the SLAC model enzyme is studied using a RRDE setup. Amino acid mutations around the T1 copper active site led to decreased enzymatic activity in all mutations tested (both single and double amino acid mutants) and lower ORR currents (< 33% of the current observed in the $SLAC_{WT}$). In all the mutants, the half-wave potential shifted from that of the $SLAC_{WT}$. Only two mutants were observed to have greater $E_{1/2}$ than $SLAC_{WT}$, T232V ($p= 0.7$) and M198L-T232V ($p= 0.8$). Due to

slow enzyme kinetics, the RRDE results did not show differences in the ORR currents between 400 and 1600 rpm and therefore the kinetics of the SLAC mutants were not able to be analyzed using typical RRDE approaches. However, the $SLAC_{WT}$, having faster kinetics, was able to be analyzed using the Koutecky-Levich and charge/mass balance approach and indicated a two electron charge transfer mechanism with a kinetic rate constant of 9.14×10^{-5} cm/s.

Chapter 6 – Mechanistic study of DET in bilirubin oxidase

6.1 Introduction

Multi-copper oxidase (MCO) is a family of enzymes, evolutionarily and structurally related, involved with pigmentation, morphogenesis, detoxification, and lignin degradation. This family of enzymes includes ascorbate oxidases, laccases, nitrite reductases, cuprous oxidases, ceruloplasmin (also known as ferroxidases), and bilirubin oxidases found in plants and fungi [77-79]. The majority of MCO's contain four copper active sites (per monomer of a protein molecule) consisting of one copper ion at the T1 or blue site and three copper ions at the trinuclear cluster or T2/T3 sites [58, 78, 80]. This family of enzymes reduces dioxygen to water while simultaneously oxidizing, in a one electron oxidation, the reducing substrate [67, 81-83]. Much research has been devoted to unveiling the mechanism of oxygen reduction reaction by MCO's in solution [58, 67, 75, 81-82, 84-89]. It has been shown that the reduction to water takes place on the T2/T3 site, and no free hydrogen peroxide has been registered as evolving product. It has been postulated that 4-electron mechanism is thus prevalent and this understanding has been transformed to all electrochemical systems involving MCO and demonstrating direct electron transfer [75, 90]. While there are many advances being made in incorporating MCO into biofuel cathodes, it has not been explicitly confirmed whether the mechanism of oxygen reduction in MCOs such as Bilirubin oxidase (BOD) is a four electron transfer [12, 50, 54, 91-92]:

$$O_2 + 4H^+ + 4e^- \rightarrow 2H_2O \qquad 1.23 \text{ V vs. NHE} \qquad (8)$$

or a two-electron transfer with a hydrogen peroxide intermediate (Figure 6.1) [93-94]:

$$O_2 + 2H^+ + 2e^- \rightarrow H_2O_2 \qquad 0.68 \text{ V vs. NHE} \qquad (9)$$

$$H_2O_2 + 2H^+ + 2e^- \rightarrow H_2O \qquad 1.77 \text{ V vs. NHE} \qquad (10)$$

The formation of H_2O_2 decreases the number of electrons transferred per molecule of O_2 reacted and is hard on biological entities making the four-electron, direct transfer mechanism more desirable. This research aims to clarify the mechanism of oxygen reduction in the MCO enzyme BOD.

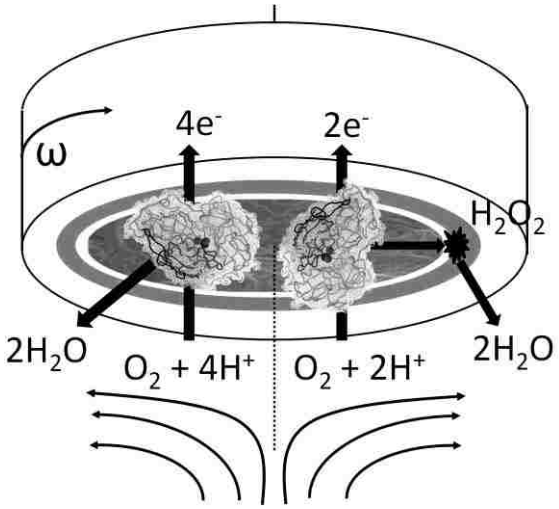

Figure 6.1 - Four- and two-electron transfer on the carbon nanotube coated rotating ring-disc electrode.

It is a task of this study to establish the number of electrons exchanged in BOD-catalyzed oxygen reduction reaction (ORR) by a standard electrochemical technique and to confirm the absence of hydrogen peroxide as a free intermediate corresponding to a 4-electron transfer mechanism. The mechanism for oxygen reduction was studied using electrochemical measurements carried out on a rotating ring disc electrode (RRDE) with an inert (glassy carbon) disc electrode. The disc was modified by a thin film containing the enzyme catalysts and used for measuring the oxygen reduction reaction. The catalytic Pt ring electrode simultaneously measures a second reaction, the decomposition of hydrogen peroxide at constant potential [95]. In this work, the catalyst, BOD was deployed on the disk in a form of an ink (suspension) of multi-walled carbon nanotubes (MWNT), with the enzyme immobilized onto their surface and dispersed in alcohol/water suspension of tetrabutylammonium bromide (TBAB) modified Nafion™, Figure 6.2.

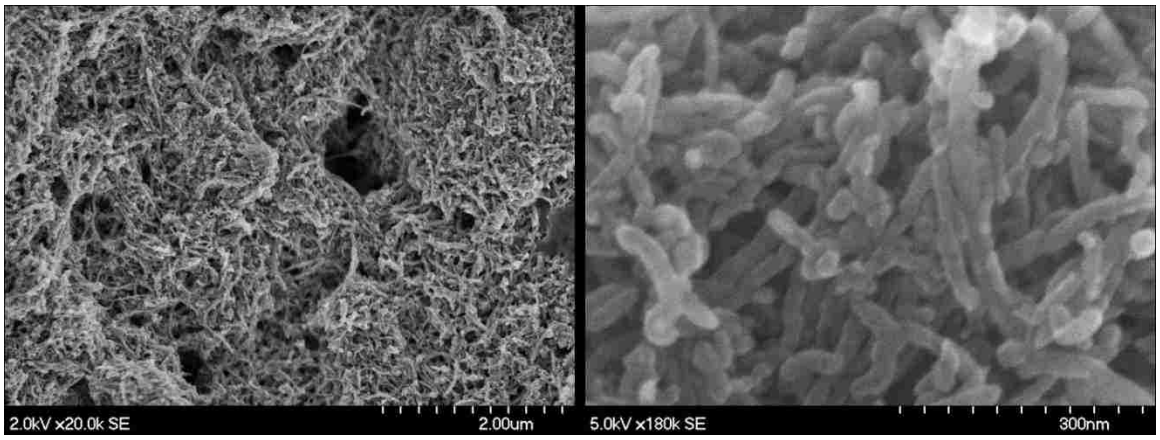

Figure 6.2 - SEM of dropcast ink containing single walled carbon nanotube, tetrabutylammonium bromide (TBAB) modified Nafion™, 1-pyrenebutanoic acid, succinimidyl ester (PBSE), and bilirubin oxidase on glassy carbon. Scale bar 2 um (left) and 300 nm (right).

6.2 Experimental

6.2.1 Glassy carbon disc electrode preparation

The RRDE was cleaned with alumina, 1 μm, 0.3 μm, followed by 0.05 μm grit with a washing of water in between each grit. A suspension of 5% multi-walled carbon nanotube (MWNT obtained from cheaptubes.com) in 4:1 water: ethanol suspension (reagent grade, Sigma, St. Louis, MO) was bath sonicated for 30 minutes. The MWNT suspension was then reacted with 10 mM 1-pyrenebutanoic acid, succinimidyl ester (PBSE), 10 mg/ml bilirubin oxidase (BOD). Then one of two polymers was then added to the MWNT suspension:

- Chitosan polymer, 0.5% in 0.3 M acetic acid, or

- TBAB-Nafion polymer, 0.1% in absolute ethanol, a gift from the laboratory of Prof. Shelley Minteer, St. Louis University, MO [96-97].

The MWNT suspension, containing BOD attached to MWNT through a PBSE linker, requires a binder to attach to the glassy carbon electrode. The drop-casting method relies on evaporation of the MWNT suspension to coat the electrode. Chitosan and TBAB-Nafion polymers were found to produce successful MWNT suspension attachment to the electrode and be enzyme compatible [98-99]. Chitosan, a linear polysaccharide formed from deacylated chitin obtained from crustaceans, is well known for being biocompatible, biodegradable, chemically inert, non-toxic, and having high mechanical strength.[100-103]. TBAB-Nafion, a derivative of Nafion made by exchanging the proton in the sulfonic acid group for a tetra-alkylammonium cation (TBAB), exhibits increased pore size, increased hydrophobicity, and decreased acidity [96]. The larger pore size increases mass transport and enzyme encapsulation in an enzyme compatible environment [8, 96, 104-105].

The MWNT suspension (regardless of the polymer uses) was incubated at 4^{o} C for 50 minutes. Then 10 μL of the suspension was dropcast on the glassy carbon disc and dried under nitrogen gas. Under this procedure the loading of the "catalysts", BOD-modified MWNT, was 0.40 mg/cm^2.

6.2.2 Electrochemical measurements of ORR activity

Electrochemical measurements were using a three-electrode setup, the working electrode was a RRDE, the reference electrode was Ag/AgCl and the counter electrode was a platinum wire. The disc potential was swept from +0.8 to 0.0 V (in cathodic direction) at

a scan rate of 10 mV/s (optimized to yield the highest ORR currents) while the potential at the ring was held constant at +0.8 V. Using the oxygen reduction reaction theory, the potential of 0.8V was chosen because it is just below the potential where water begins to split, which was determined experimentally for the buffer used [106-107]. The optimum scan rate for the RRDE measurements was determined by varying the scan rate and measuring the corresponding observed oxygen reduction reaction (ORR) currents, Figure 6.3 (left). The largest ORR currents are observed for scan rates of 10 mV/s. The supporting electrolyte was 100 mM potassium phosphate at pH 7.5. Electrochemical measurements are taken under oxygen or nitrogen saturated conditions with the gas was bubbling through the cell at room temperature.

Bilirubin oxidase (BOD) is covalently linked to 1-pyrenebutanoic acid succinimidyl ester (PBSE), which is non-covalently tethered to multi walled carbon nanotubes (MWNT) [108]. An ink of such BOD-modified MWNT is made by suspending them in an aqueous polymer solution containing tetrabutyl-ammonium bromide (TBAB) modified Nafion™. This ink is then drop cast on the glassy carbon disc of the rotating electrode and dried at room temperature under nitrogen gas.

6.3 Results and Discussion

6.3.1 Chitosan and TBAB-Nafion Polymer Comparison

Activity of BOD co-dropcast with MWNT, PBSE, and one of two polymers, TBAB-Nafion or Chitosan, is compared in the cyclic voltammograms (CV) in Figure 6.3 (right). CVs that utilize chitosan as the polymer are shown under nitrogen saturated conditions

(j), oxygen saturated conditions at 0 rpm (j) and 500 rpm (l) rotation rate. The CVs with TBAB-Nafion polymer are shown under nitrogen saturated conditions (g), oxygen saturated conditions at 0 rpm (h) and 500 rpm (i) rotation rate. The ORR onset potential is 0.5 V, regardless of the polymer used. The ORR currents observed and limiting current at 0 V differs between the TBAB-Nafion and chitosan polymer utilizing systems.

BOD activity with chitosan as the polymer resulted in a small ORR current density, 105 ± 8 $\mu A/cm^2$ (Figure 6.3, right). The corresponding orientation efficiency was calculated to be 0.0020 ± 0.0001 % and the electrochemically accessible surface area was calculated to be 156 ± cm^2. BOD activity with TBAB-Nafion as the polymer resulted in an ORR current of 103 ± 5 μA on the disc (Figure 6.3, right). The orientation efficiency was calculated to be 0.0076 ± 0.0004 % and the ECSA was calculated to be 518 ± 5 cm^2. The ORR current and electrochemically accessible surface area (ECSA) were calculated using currents obtained at 300 mV.

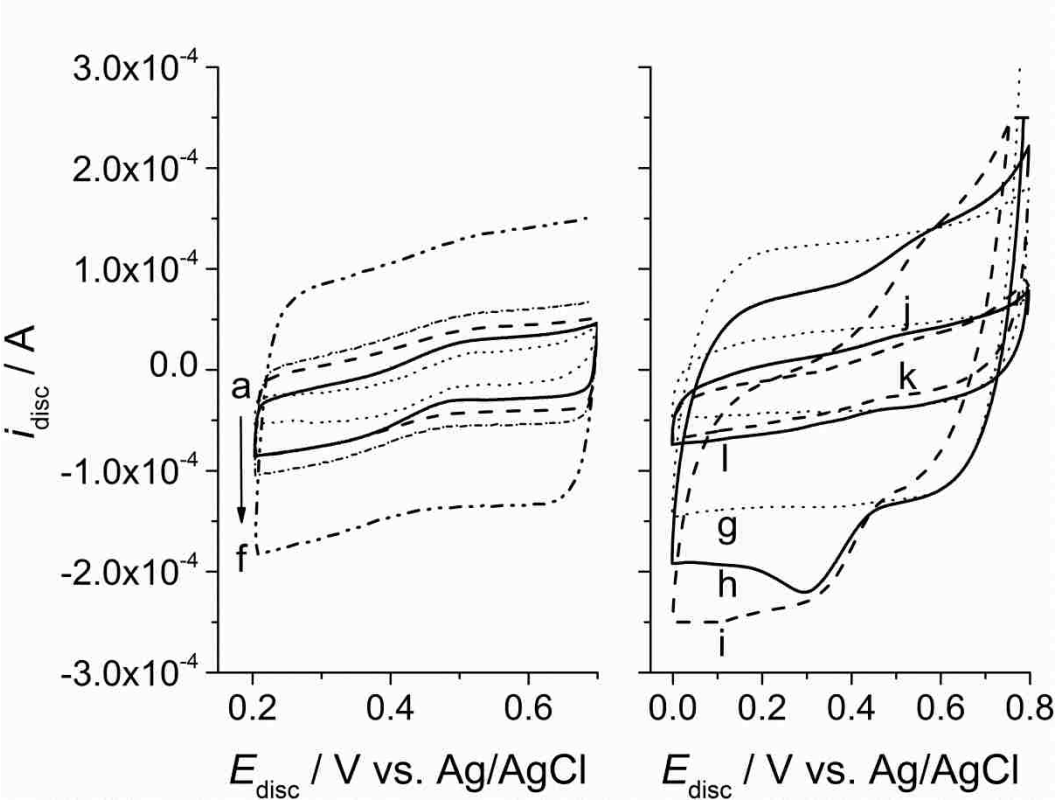

Figure 6.3 - [left] Optimum scan rate for RRDE measurements was determined by varying the scan rate (a) to (f) corresponding to 5 mV/s, 10 mV/s, 15 mV/s, 20 mV/s, 50 mV/s, and 100 mV/s scan rates, respectively, (0.1 M potassium phosphate buffered at pH 7.5). [right] TBAB-Nafion polymer, 0.1%, (g- N_2, 0 rpm, h- O_2, 0 rpm, i- O_2 500 rpm) or chitosan polymer, 0.5%, (j- N_2, 0 rpm, k- O_2, 0 rpm, l- O_2 500 rpm) aided MWNT suspension attachment to disc electrode (100mM potassium phosphate buffered at pH 7.5). RRDE disc potential was swept from 0.8 V to 0.0 V at a scan rate of 10 mV/s while the ring was polarized at 0.8 V.

The TBAB-Nafion polymer, when compared to chitosan, leads to greater oxygen reduction currents, larger ECSA, and better enzyme orientation efficiency making it the superior polymer for aiding the attachment of the MWNT suspension to the glassy carbon electrode. The electrochemical current is four times greater with TBAB-Nafion than with chitosan. Both of the polymers are porous, hydrophobic, and enzyme compatible but differ in charge at experimental pH 7.5 which can explain the difference in observed ORR current. BOD has an isoelectric point of pH 4.2 which means that the enzyme is slightly negatively charged at the experimental pH 7.5 [109]. The amino group in chitosan has a pK_a value of 6.5 which leads to deprotonation at pH 7.5 making the chitosan slightly negatively charged [110]. Therefore, it is inferred that chitosan and BOD would repel each other. This results in decreased assistance from the chitosan in BOD orientation and DET leading to the observed low ORR current. Contrastingly, TBAB-Nafion, with its quaternary ammonium salt, has a positive charge regardless of the solution pH. The negatively charged BOD will be attracted to the TBAB-Nafion and it is this interaction that is hypothesized to increase the orientation efficiency allowing for DET and resulting in the observed ORR current.

6.3.2 DET Mechanism for BOD using RRDE

The mechanism of DET for BOD is investigated using a RRDE experiments. The disc of the RRDE contains the dropcast BOD linked to MWNT through PBSE and the TBAB-Nafion polymer. The dropcast TBAB-Nafion/MWNT layer covers the glassy carbon electrode completely, is mechanically very stable, and can only be removed by polishing the electrode. The rotation rate of the RRDE was varied between 0 rpms (2) and 1500

rpms (9), Figure 6.4. Disc potential was swept from 0.8 V to 0 V, the ring was polarized at 0.8 V, and the scan rate was 10 mV/s. The ORR onset potential is 0.5 V regardless of the rotation rate. As the rotation rate increases, the limiting current of the disc at 0 V increases. Variations in currents observed at various rotation rates decrease with increasing rotation rates, Figure 6.4 inset. BOD is not active enough to ensure diffusion limited current at rotation rates greater than 200 rpm resulting in the observed ORR currents that do not reach a limiting current (Figure 6.4). This phenomenon is associated with thick layers and slow catalysts [111-113]. We have not made any background corrections to the RRDE data; we present un-altered data to demonstrate the principle.

The O_2 mass transport defined plateau of the current is a function of the angular velocity of the rotating electrode below about 200 rpms (2-5). Above 200 rpms (6-9), the plateau is defined by the kinetics of O_2 reduction. The corresponding ring currents for all rotation rates are the same as the background current and do not indicate any hydrogen peroxide decomposition on the ring. The system under nitrogen saturated conditions is taken as background current since no oxygen reduction is occurring (1). These results support a four electron transfer mechanism since there was effectively zero hydrogen peroxide was detected on the ring.

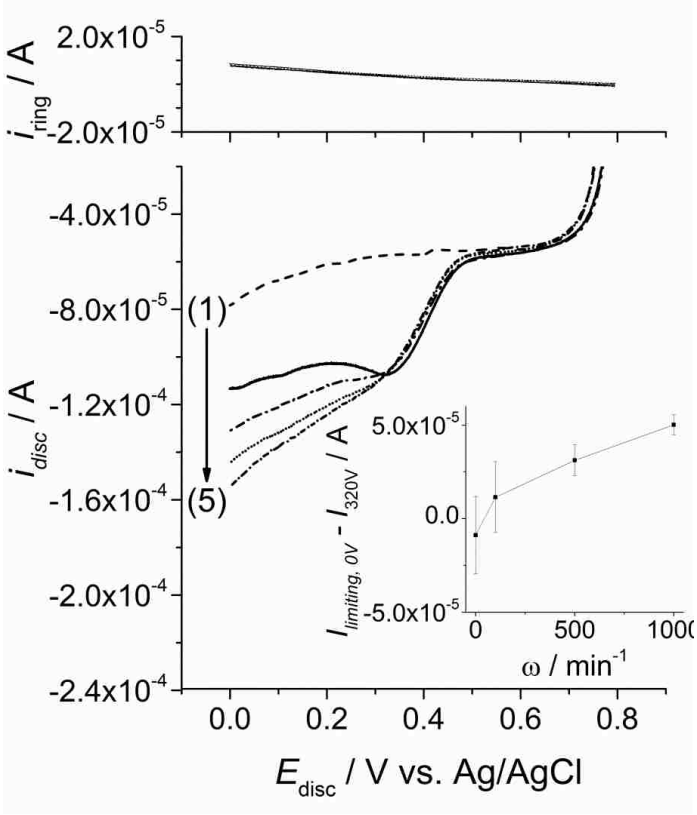

Figure 6.4 – RRDE results for the bilirubin oxidase TBAB-Nafion polymer system. Linear scan voltammetry from 0.8 V to 0.2 V (bottom) and a plot of the ring current, polarized at 0.8 V (top), versus the disc potential at various RRDE rotation rates (1) to (5) corresponding to 0 RPM under nitrogen, 0 RPM, 100 RPM, 500 RPM, and 1000 RPM, rotation rates, respectively, under oxygen saturated conditions unless otherwise stated (0.1 M potassium phosphate buffered at pH 7.5). (Data not shown for 50 RPM, 150 RPM, 200 RPM, and 1500 RPM for clarity.) Inset, baseline corrected variations in current demonstrate reproducibility at various rotation rates. Variability in the observed currents between duplicate experiments decrease as the rotation rate increases.

6.3.3 Koutecky-Levich Analysis

The Levich plot of limiting current versus the angular rotation rate of the RRDE is plotted in Figure 6.5 (top). The linear region, angular velocity below ~6/s (200 rpm) corresponds to the Levich region where oxygen is freely diffusing to the electrode surface implying that the kinetic reaction is faster than the rate of substrate delivered to the electrode. The nonlinear region corresponds to the non-Levich regions where the rotation rates are too high to allow for free oxygen to diffuse the electrode surface due to turbulence caused by rotation, rotation rates above ~6 rads/s.

Increased RRDE rotation rates lead to a faster supply of oxygen to the electrode surface and greater turbulence near the electrode surface which both affect the oxygen diffusion to the electrode surface.

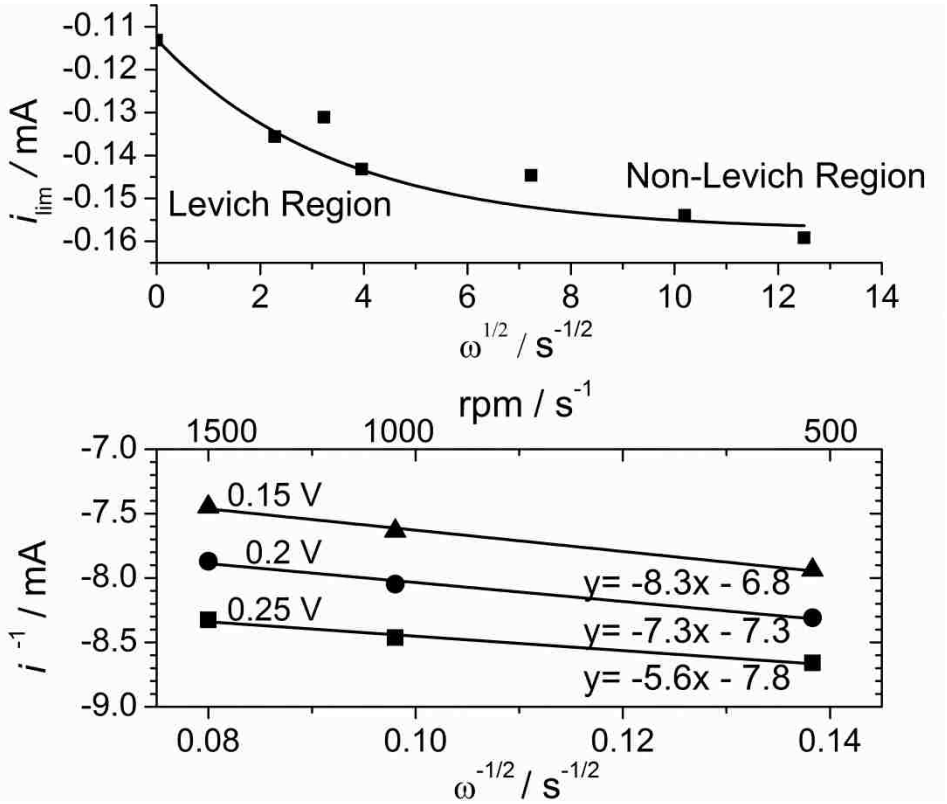

Figure 6.5 - [Top] Levich plot of limiting current plotted against angular rotation rate of the RRDE. [Bottom] Koutecky-Levich plot from which the kinetic constant, k, (y-intercept) and the number of electrons transferred per molecule of oxygen (slope) is calculated.

The Koutecky-Levich plot of the inverse current versus the inverse angular rotation rate is plotted in Figure 6.5 (bottom). Parallel, linear lines are obtained with currents at potentials 0.25 V, 0.2 V, and 0.15V, as expected. The slope and y-intercept is obtained using the straight line equation for rotations rates in the range from 500 rpm to 1500 rpm. The slopes are similar, 7.1 ± 1.2 /(mA $s^{1/2}$) and the average y-intercept is 7.3 ± 0.5 /mA indicating that the number of the electrons transferred per oxygen molecule is

3.92 ± 0.05 electrons and the kinetic rate constant is calculated to be k = 1.16 x 10^{-3} ± 0.08 x 10^{-3} cm/s.

6.3.4 DET mechanism analysis using charge/mass balances

The number of electrons calculated using the charge/mass balances averages 3.7 ± 0.2 electrons over all rotation rates which corresponds to only 7.5 ± 5% of oxygen reduction via the 2 electron pathway with the hydrogen peroxide intermediate, Figure 6.6.

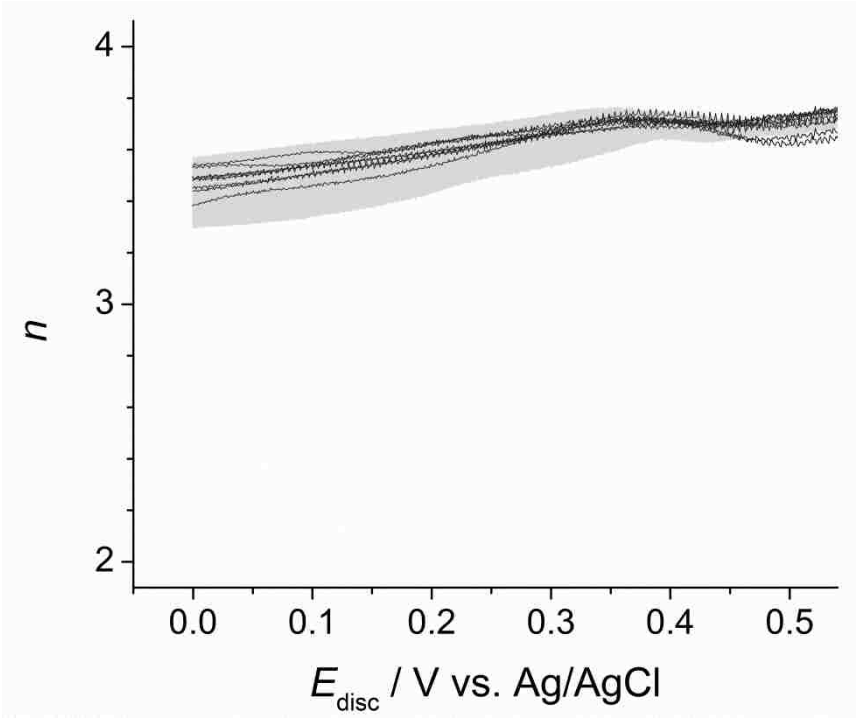

Figure 6.6 - Number of electrons transferred per molecule of oxygen (n) calculated from the mass and charge transfer balance versus disc potential at rotation rates from 0 rpm to 1500 rpm.

6.4 Conclusions

TBAB-Nafion is preferred as a binder over chitosan because it confers increased ORR current, ECSA, and enzyme orientation efficiency for the BOD enzyme. RRDE experiment results indicate a four electron DET mechanism based on the absence of hydrogen peroxide detected on the ring regardless of the rotation rate, the Koutecky-Levich and mass/charge transfer calculations. BOD has a four electron transfer mechanism without a hydrogen peroxide intermediate. This research is published in Electrochimica Acta, 2012:

Brocato, S., C. Lau, and P. Atanassov (2012). "Mechanistic study of direct electron transfer in bilirubin oxidase." Electrochimica Acta **61**: 44-49.

Chapter 7 – pH dependence of catalytic activity for ORR of non-PGM catalyst

7.1 Introduction

Currently, one of the major challenges in the commercialization of proton exchange membrane (PEM) fuel cells is high cost due in large part to the expensive platinum-based catalysts [114-117], accounting for nearly half the cost of the fuel cell stack [118]. Developing alternative, less expensive catalysts to reduce the need for Pt is a necessary approach for widespread deployment of PEM fuel cell technology [119]. One solution is to replace the Pt-based catalysts with non-precious metal catalysts at the oxygen-reducing cathode thereby reducing the Pt content by a factor of 10 fold [120].

In recent year, there has been increased research on non-platinum group metal catalysts such as pyrolyzed Fe- and Co- based nitrogen containing complexes, transition metal chalcogenides, transition metal oxides/carbides/nitrides/oxynitrides/carbonitrides, and pyrolyzed transition metal nitrogen containing complexes supported on carbon materials (Fe- or Co-N_x/C), the latter being considered most promising because of demonstrated ORR activity and stability [121-122]. All of these recent achievements in non-platinum group metal catalysts for ORR were summarized in the literature review [120, 123-124].

Unfortunately, the mechanism for the ORR on these new catalysts has not been well studied or characterized over a full range of pHs. The little data we have comes from acidic or basic media. There is very little data on the ORR mechanism in neutral media, necessary for the incorporation of enzymes into fuel cells. The oxygen reduction is

theorized to occur via a four electron transfer or a two-electron transfer with a hydrogen peroxide intermediate. The formation of H_2O_2 decreases the number of electrons transferred per molecule of O_2 reacted making the four-electron, direct transfer mechanism more desirable.

Understanding the ORR mechanism is of paramount importance because of its role in electrochemical energy conversion. In this research we analyze the ORR mechanism for Fe-phenanthroline over the full pH range from 1 to 14 using electrochemical measurements carried out on a rotating ring disc electrode (RRDE) with an inert (glassy carbon) disc electrode and a platinum ring. The disc was modified by a thin film containing Fe-phenanthroline and used for measuring the oxygen reduction reaction. The aim of this work is to elucidate the ORR mechanisms over the full pH range and determine if the oxygen reduction mechanism shifts as a result of pH change. This knowledge has applications in both PEM fuel cells, anion exchange membrane (AEM) fuel cells, and for incorporation of enzymes into fuel cells.

7.2 Experimental

7.2.1 Fe-phenanthroline synthesis

Fe-phenanthroline catalysts were prepared by sacrificial support method (SSM) utilizing wet impregnation of iron and 1,10-phenanthroline precursors onto the surface of fumed silica (Cab-O-Sil™ EH-5, surface area: ~400 m^2/g). First, calculated amount of silica (the total metal loading on silica was calculated as ~15wt.%) was dispersed in water on ultrasound bath. Then a solution of 1,10-phenanthroline (1,10-phenanthroline, Sigma-

Aldrich) in acetone was added to silica and sonicated for 20 minutes. Finally, solution of iron nitrate ($Fe(NO_3)_3*9H_2O$, Sigma-Aldrich) was added to SiO_2-phenanthroline solution and sonicated for 8 hours. After sonication, viscous solution of silica and Fe-phenanthroline was dried overnight at T=85°C. Obtained solid was ground until fine powder in agate mortar and used for heat treatment (HT). The general conditions of HT were: UHP nitrogen with flow rate 100 cc/min, HT temperature was 800°C, heat treatment ramp was 3 deg/min.

Iron to phenanthroline ratio initially was selected as Fe:phenanthroline = 1:4 (mass), and the catalyst was denoted as Fe-4Phenanthroline. SEM images of Fe-4Phenanthroline are presented in Figure 7.1. The chemical composition of Fe-phenanthroline after synthesis is approximately 2 wt.% Fe, 3 wt.% N, and 95 wt.% C.

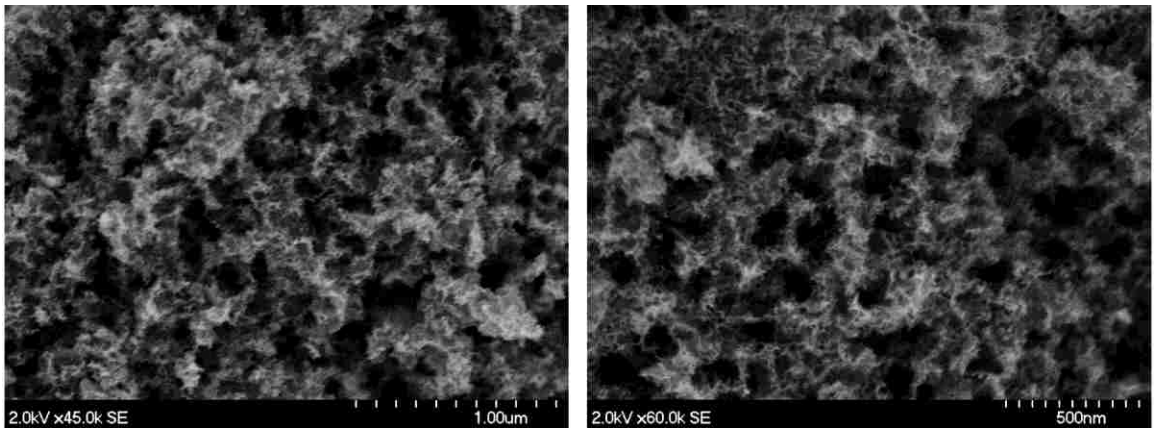

Figure 7.1 – SEM image of Fe-4Phenanthroline. Scale bar: 1µm (left) and 500 nm (right).

7.2.2 Solution preparation of various pHs

A solution of 0.5 M sulfuric acid (Sigma, St. Louis, MO) was used for pH 1. A pH adjusted solution of 0.5 M sulfuric acid and 0.1 M potassium phosphate (EMD Chemicals, Gibbstown, NJ) was used for pH 2 and pH 3. A buffered solution of 0.1 M potassium phosphate (EMD Chemicals, Gibbstown, NJ) was used for pH 4 through pH 8. A pH adjusted solution of 1 M potassium hydroxide (Sigma, St. Louis, MO) and 0.1 M potassium phosphate (EMD Chemicals, Gibbstown, NJ) was used for pH 9 through pH 13. A solution of 1 M potassium hydroxide (Sigma, St. Louis, MO) was used for pH 13.7. The pHs of all the solutions, pH 1 through 13.7, were stable and confirmed using an Omega PHB600R pH meter.

7.2.3 RRDE electrochemistry

Electrochemical measurements were performed in a 125mL glass electrochemical cell using a WEB30-Pine bipotentiostat and a Pine Instruments Rotator (Pine Instruments, Raleigh, NC). A three electrode setup was used, the reference electrode was Ag/AgCl for pH 1 through pH 7 and Hg/HgO for pH 8 through pH 13.7 and the counter electrode was a platinum wire. The disc potential was swept from 1.0 V to 0.2 V vs. RHE and the ring was polarized at 1100 mV for pH 1 through pH 7 and at 600 mV for pH 8 through pH 13.7. The potentials measured vs. the reference electrode were converted to RHE. The conversion factor was determined using a platinum working electrode vs. the reference electrode (Ag/AgCl or Hg/HgO) for each pH 1 through 13.7. This method was deemed to be more accurate for our system than using published reference electrode conversion

values, although the conversion values obtained were similar. The scan rate was 10mV/s. Electrochemical measurements were taken under oxygen saturated conditions with the gas bubbling through the cell at room temperature and ambient pressure.

Working electrodes were prepared by mixing 5 mg of the Fe-Phenanthroline electrocatalyst with 850 μL of a water and isopropyl alcohol (4:1) mixture, and 150 μL of Nafion® (0.5% wt., DuPont). The mixture was sonicated before 30 μL was applied onto a glassy carbon disk with a sectional area of 0.2472 cm^2. The loading on the working electrode was adjusted by deposition of calculated amount of ink to obtain 50, 200, and 600 $\mu g/cm^2$ catalyst on the electrode.

7.3 Inner- and outer-sphere electron transfer mechanisms

The inner-sphere electron transfer mechanism (Figure 7.2, a) occurs in both acidic and alkaline media when molecular oxygen chemisorbs on to the Fe-phenanthroline active sites followed by a 4 e^- / 4 H^+ transfer [51, 125]. In this mechanism, all of the reaction intermediates remain adsorbed on the active site until the final product is desorbed into the bulk. The inner-sphere electron transfer reaction mechanism in alkaline media:

$$O_2 \rightarrow O_{2,\,ads} \tag{3}$$

$$O_{2,\,ads} + H_2O + 2e^- \rightarrow (HO_2^-)_{ads} + OH^- \tag{4}$$

$$(HO_2^-)_{ads} + H_2O + 2e^- \rightarrow 3OH^- \tag{5}$$

The outer-sphere electron process (Figure 7.2, b) occurs only in alkaline media when solvated molecular oxygen and water cluster weakly interact with surface adsorbed hydroxyl molecules (stabilized through hydrogen bond formation), leading to a two electron transfer pathway to HO_2^- [51, 125]. The outer-sphere electron transfer reaction mechanism in alkaline media:

$$Me\text{-}OH + [O_2 \cdot (H_2O)_n] + e^- \rightarrow M\text{-}OH + (HO_2^{\cdot})_{ads} + OH^- (H_2O)_{n-1} \quad (6)$$

$$(HO_2^{\cdot})_{ads} + e^- \rightarrow (HO_2^-)_{ads} \quad (7)$$

$$(HO_2^-)_{ads} \rightarrow (HO_2^-)_{aq}. \quad (8)$$

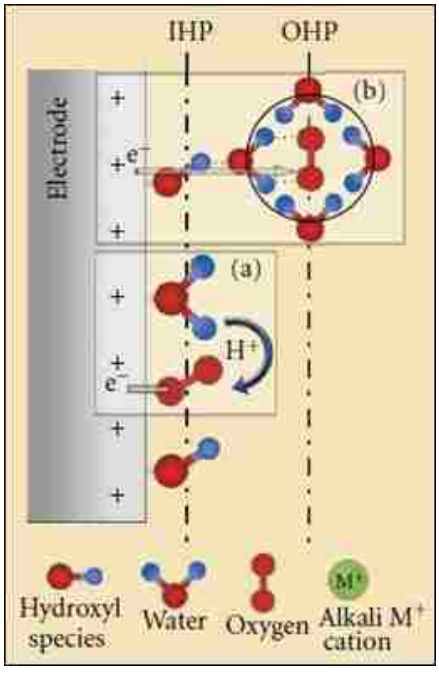

Figure 7.2 - Schematic of the double-layer structure during ORR in alkaline media illustrating (a) the inner- and (b) the outer-sphere electron transfer processes [125].

7.4 Results and Discussion

7.4.1 RRDE

To test the effect that pH had on the direct electron transfer mechanism of Fe-phenanthroline, electrochemical techniques were employed for characterization. The Fe-4Phenanthroline catalyst was tested in various pH solutions, from pH 1 to pH 13.7. The current-potential curves were obtained at various rotation rates from 400 rpm to 1600 rpm in oxygen saturated solution. Figure 7.3 shows RRDE linear scan voltammetry taken at 1600 rpm and a scan rate of 10 mV/s. The pHs presented provide a representative sample for the trends observed for pH 1-13.7.

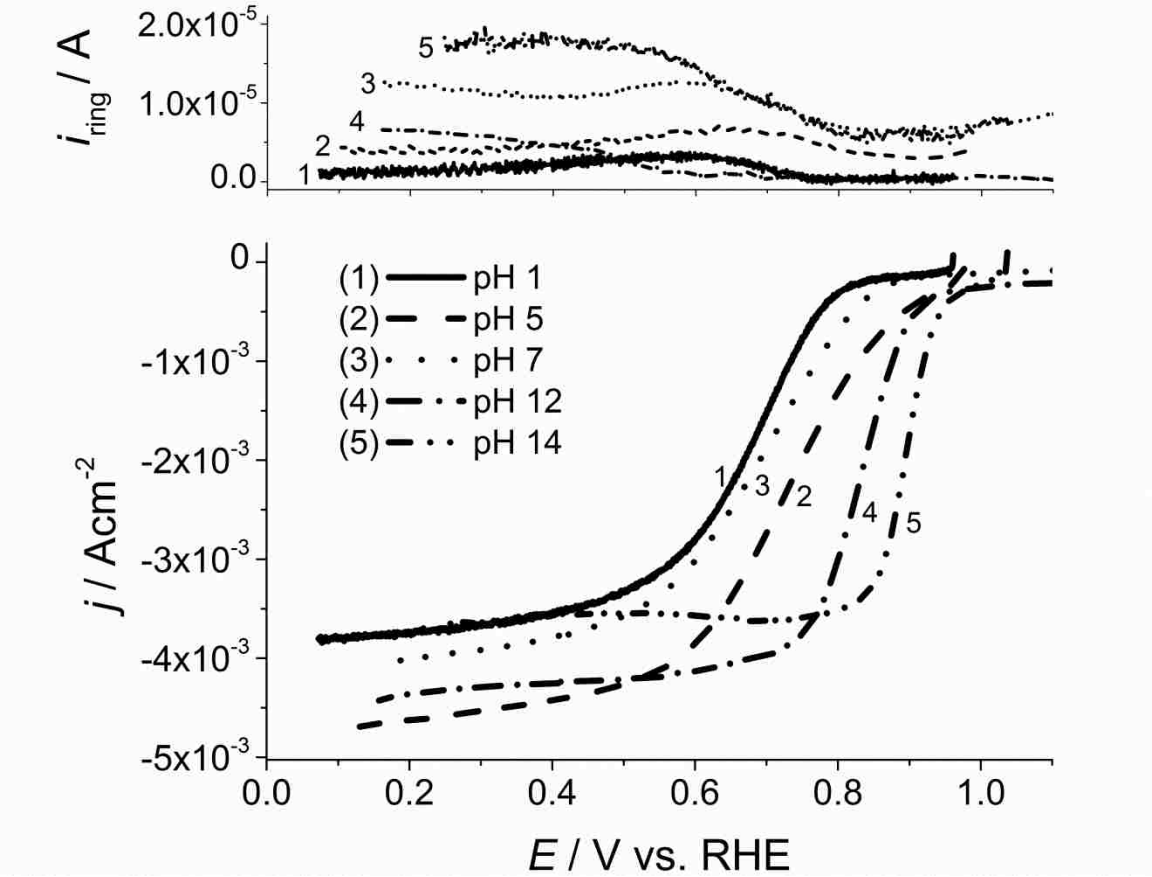

Figure 7.3 – Fe-4Phenanthroline linear scan voltammetry from 1.0 V to 0.2 V (bottom) and the corresponding ring currents versus the disc potentials at 1600 rpm rotation rate (top). For clarity only a representative pH data set is shown.

The half-wave potential ($E_{1/2}$) is observed to remain steady at approximately 0.7 V from pH 1 to pH 7, linear slope is 2.8 ± 2.5 mV/pH, and increase linearly from pH 7 to pH 13.7, linear slope is 26.5 ± 5.0 mV/pH, Figure 7.4 (middle). The half-way potential was determined by using the second derivative method. The rate limiting step in acidic media does not depend on pH or the concentration of H^+. On the contrary, in alkaline media the rate limiting step is dependent on the hydroxyl concentration and a slope of approximately 30mV/pH indicate that the first electron charge transfer step is rate

limiting. Additionally, the hydrogen peroxide intermediate in alkaline media, HO_2^-, has higher stability on the Fe^{2+} active than the intermediate in acid media, H_2O_2, and partially contributes to the increased half-wave potential.

7.4.2 Percent hydrogen peroxide

The amount of hydrogen peroxide generate from Fe-phenantroline is calculated to be less than 5% for all pHs, Figure 7.4 (top). The maximum hydrogen peroxide production occurring at pH 14 (5.0 ± 0.2 $\%H_2O_2$) is a result of a shift in the mechanism from an inner electron sphere process to a combination of inner and outer electron sphere processes. The percent hydrogen peroxide generated in alkaline media is kept low despite increasing OH^- substrate concentration due to two processes that lead to a $4e^-$ transfer mechanism: hydroxyl species adsorbed on the Fe-phenanthroline surface that are easily displaced by molecular oxygen leading to less adsorbed hydroxyl species to participate in the outer sphere reaction and enhanced activation of the peroxide intermediate on the Fe^{2+} active site [125].

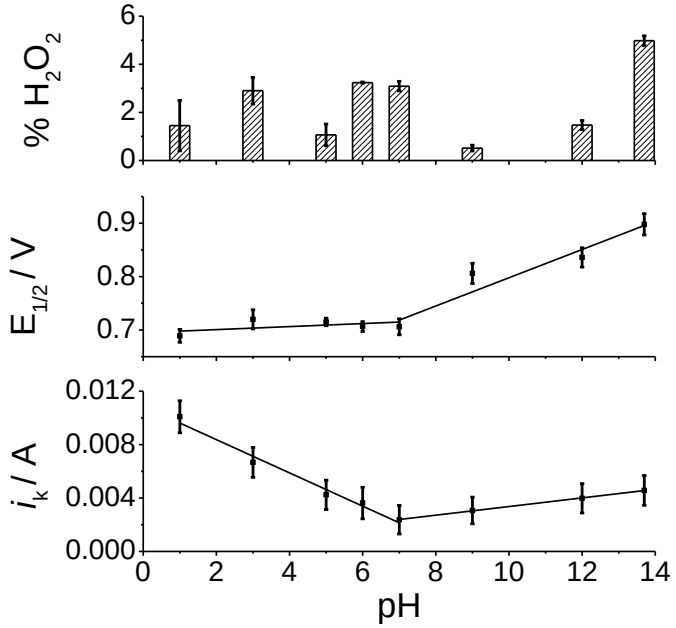

Figure 7.4 - The percent hydrogen peroxide detected on the ring (top). The half-way potential for oxygen reduction in Fe-4Phenantroline (middle). The kinetic current, i_k, (bottom) at pH ranging from 1 to 13.7 obtained from the Koutecky-Levich analysis.

7.4.3 Charge/mass balance analysis

The direct electron transfer mechanism was analyzed with a charge/mass balance using the 0.3 V potential. This potential is chosen because oxygen reduction reaction has reached steady state at all pHs. The charge/mass balance analysis method utilizes the ring and disc current to obtain n, requiring that the hydrogen peroxide be directly detected on the ring if a 2 electron transfer mechanism is to be measured.

Figure 7.5 illustrates the number of electrons calculated per molecule of oxygen, n, versus pH at 3 different loadings, 50 μg/cm^2 (low), 200 μg/cm^2 (mid), and 600 μg/cm^2

(very high) calculated using the charge/mass balance method. The number of electrons transferred per molecule of oxygen (n) remains steady, over the entire pH range, at 3.90 ± 0.07 and 3.90 ± 0.09 e^- for 200 μg/cm^2 and 600 μg/cm^2, respectively. The 50 μg/cm^2 loading remains steady at 3.90 ± 0.05 e^- for pHs 1 through 12 and then sharply decreases to 3.01 ± 0.03 e^- at pH 13.7, a result of the un-uniform coating on the disc resulting from the extremely low loading. From these results, we determine that the 50 μg/cm^2 loading is too low for the Koutecky-Levich analysis. Conversely, the 600 μg/cm^2 loading is too high for the Koutecky-Levich analysis creating loading creates a very thick, porous catalyst layer, limiting diffusion at the electrode surface, and trapping intermediates (hydrogen peroxide) within the catalyst. The fundamental limitations of the Koutecky-Levich equation restrict its use to systems under complete kinetic control which ultimately limits its use to ultra thin catalyst layers where diffusion at the electrode surface is not constrained. The 200 μg/cm^2 loading creates a uniform, not-too-thick catalyst layer on the disc and therefore, is used for the Koutecky-Levich analysis.

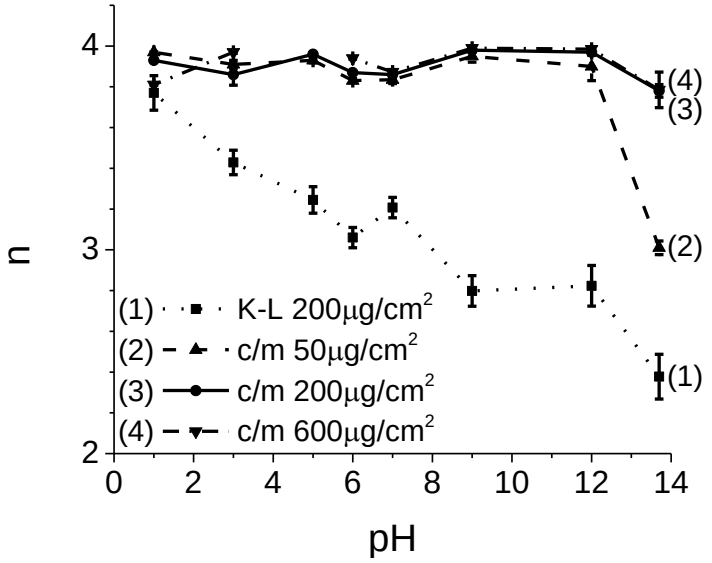

Figure 7.5 - Number of electrons transferred per molecule of oxygen (n) determined using the Koutecky-Levich analysis at (1) 200 μg/cm^2 loading and the charge/mass balance at (2) 50 μg/cm^2, (3) 200 μg/cm^2, and (4) 600 μg/cm^2.

7.4.4 Koutecky-Levich analysis

The RRDE linear scan voltammetry curves presented in Figure 7.3 were analyzed using the Koutecky-Levich theory. Figure 7.6 shows the Koutecky–Levich plot based on data at 0.3V vs. RHE. For comparison two theoretical lines for 2- and 4-electron transfer processes under complete diffusion-controlled conditions are also given in Fig. 5. For very alkaline pHs, pH 12 and greater, the catalyst was too active to attain diffusion-controlled conditions at the lowest rotation rate tested, 400 rpm, therefore no data points are presented in the Koutecky-Levich plot, Figure 7.6, corresponding to pH 12 and pH 14 at 400 rpm.

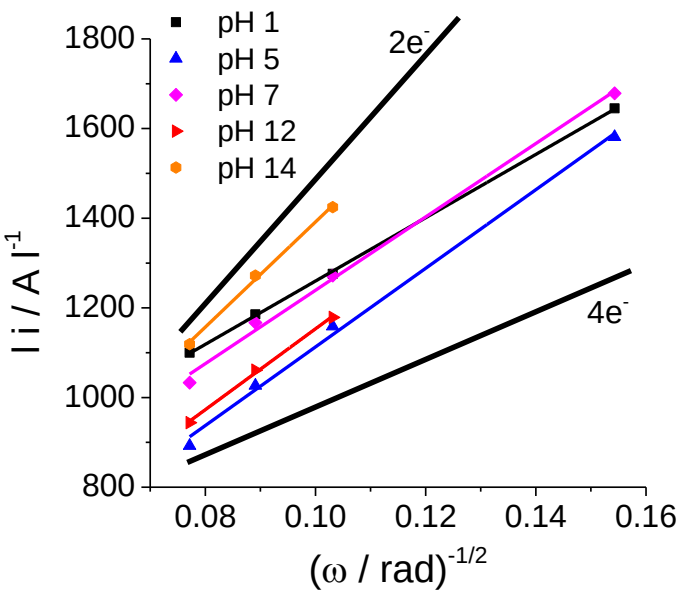

Figure 7.6 - Koutecky-Levich plot from which the kinetic current (i_k) and the number of electrons transferred per molecule of oxygen (n) were calculated. Fe-4Phenanthroline loading is 200 µg/cm^2. A representative sample of the results is shown.

Using the slopes obtained from the Koutecky-Levich plot, the average number of electrons transferred per molecule of oxygen is observed to decrease with increasing solution alkalinity from 3.77 ± 0.09 e^- at pH 1 to 2.38 ± 0.11 e^- at pH 13.7 at loadings of 200 µg/cm^2 (Figure 7.6) resulting from a mechanism change occurring at pH 7 from an exclusively inner-sphere electron transfer process in acidic conditions (4e^- process) to contributions from both inner- and outer-sphere electron transfer mechanisms in alkaline media (2e^- process) [125].

The kinetic current at pHs from 1 to 13.7 are illustrated in Figure 7.4 (bottom). The kinetic current is observed to sharply, linearly decrease from pH 1 (10.1 ± 1.2 mA) to pH 7 (2.4 ± 1.1 mA) where it reaches a minimum resulting from a decrease in the concentration of protons, the reaction substrate. The slow, linear increase in the i_k from pH 7 to pH 13.7 (4.6 ± 1.1 mA) is attributed to a shift in the reaction mechanism from a purely inner electron sphere mechanism in acid media to a combination of inner and outer electron sphere processes in alkaline media [125]. The kinetic current in alkaline media does not reach the same magnitude as in acid media due to the combination of a slower outer sphere electron process and a lower concentration of hydroxyl species on the electrode surface. These results indicate that the ORR is faster in acidic media resulting from a mechanism shift occurring at pH 7.

7.5 Conclusion

The kinetics of the ORR in Fe-phenanthroline was analyzed over the entire pH 1 to pH 13.7 range using a rotating ring-disc electrode setup. Fe-phenanthroline has half-wave potential that is not dependent on pH for pH 1 to pH 7 and increases linearly with increasing pH from pH 7 to pH 13.7 where it reaches a maximum. The number of electrons transferred decreases from pH 1 to pH 13.7 according to the Koutecky-Levich analysis. The kinetic current (i_k) reaches a minimum at pH 7 indicating that the ORR rate is dependent on pH. The charge/mass balance analysis yielded the number of electrons transferred to be just under 4 electrons. The percent hydrogen peroxide generated was below 5% over all pHs at steady state potentials. The results from the half-wave potential, hydrogen peroxide generation, number of electrons transferred and kinetic rate constant,

when taken together, indicate a mechanism shift taking place at pH 7 resulting from changes in the double-layer structure and the reaction mechanism. This research has been submitted to Electrochimica Acta:

Brocato, S., A. Serov, and P. Atanassov. "pH dependence of catalytic activity for ORR of non-PGM catalyst." Electrochimica Acta, EA-S-12-02475.

Chapter 8 – Conclusions and future outlook

The goal of engineering self-assembling, multi-enzyme complexes through DNA templated assemblies is multifaceted and complicated to achieve. Multi-enzyme complexes will improve biofuel cell performance and increase current and power by bringing the active sites in close proximity to each other leading to decreased diffusion time for intermediates, increasing the concentration of intermediates around the active sites, and blocking inhibitory molecules from reaching the active sites. The research presented here provides the enabling technologies required to achieve quaternary protein structures through DNA templated assemblies.

8.1 Engineering of a redox protein for DNA-directed assembly

An engineered enzyme conjugate of the small laccase enzyme from *Streptomyces coelicolor* and zinc finger DNA binding domain from Zif268 is demonstrated to bind double stranded DNA in a site specific manner while retaining enzymatic activity. The conjugate enzyme, SLAC-3ZF, was evaluated using SPR, ABTS and DMP calorimetric assays, and MBCA. SLAC-3ZF is demonstrated to be catalytically active in both the DNA-bound and unbound states and displays site specific binding to a single specific DNA sequence. This work demonstrates a proof of concept that quaternary protein structures can be achieved through DNA templated enzyme assemblies.

8.2 Multi-copper oxidase T1 structure-function relationship investigation

The effect of amino acid mutations around the T1 copper center in SLAC were investigated in an effort to understand and improve the interfacial DET and intramolecular electron transfer from the T1 to T2/T3 site. Mutant SLAC enzymes were tested for ORR onset potential, ORR current, and $E_{1/2}$ using a RRDE. All the mutants tested had lower catalytic activity than the $SLAC_{WT}$ but two had greater $E_{1/2}$ than $SLAC_{WT}$. The $SLAC_{WT}$ was analyzed using Koutecky-Levich and charge/mass balance methods and indicated a two electron transfer mechanism. This work gives a better understanding of the structure-function relationship of the MCO T1 copper center to aid in future design of engineered MCOs for efficient biofuel cells.

8.3 Mechanistic study of DET in bilirubin oxidase

Bilirubin oxidase was studied using a RRDE setup and analyzed using Koutecky-Levich and charge/mass balance approaches to determine the amount of hydrogen peroxide generated, the number of electrons transferred per molecule of oxygen, and the electron transfer rate constant. The BOD enzyme produced no hydrogen peroxide (only background levels were detected) and has a four electron transfer ORR mechanism (no hydrogen peroxide intermediate). The preferred binder for MWNT dropcasting was determined to be TBAB-Nafion because of the increased enzyme activity it confers. The DET mechanism of the MCO bilirubin oxidase gives us a better understanding of the mechanism in the MCO enzyme family whose members share a similar four copper active site.

8.4 pH Dependence of catalytic activity for ORR of non-PGM catalyst

The non-PGM catalyst Fe-phenanthroline was used to elucidate the ORR mechanism over the full pH range to determine if and at what pH the ORR mechanism shifts. The hydrogen peroxide generated and kinetic rate constants were determined for pH 1-13.7 using RRDE experiments and Koutecky-Levich and charge/mass balance analysis methods. The ORR mechanism shift occurs at pH 7 as a result of the changing concentrations of the hydronium and hydroxide ions. The ORR reaction with OH^- proceeds slower than with H^+ as the substrate and the number of electrons transferred decreases from 3.77 ± 0.85 (pH 1) to 2.38 ± 0.11 (pH 13.7) electrons. This work clearly shows the ORR mechanism shift occurring at pH 7 and provides the first known mechanistic study of the ORR on a non-PGM catalyst over the full pH range.

8.5 Future outlook

The work presented here lays the ground work for construction of DNA-templated multi-enzyme biofuel cells and biosensors. In the future, a DNA-templated system with two or more conjugate enzymes should be investigated to demonstrate: feasibility of the DNA-template system for engineered quaternary protein structures, variability in protein-DNA attachment sites to allow for multiple site-specific enzyme attachments, and increased enzyme catalytic activity associated with metabolon like structures. The DNA-template approach to achieving self assembling, quaternary protein structures for enzymatic cascades is expected to be used to increase enzyme performance for practical applications

in vivo and *in vitro*. These applications include fuel cells that utilize glucose, glycerol, ethanol, ethylene glycol, or other complex biofuels, fuel cells and sensors that use engineered enzyme catalysts, artificial mitochondria, etc.

The investigations into the mechanism of ORR in MCO enzymes and non-PGM catalysts presented here contribute to understanding the cathodic reaction widely utilized in fuel cell technology. The knowledge presented here should be used to better characterize the reactions occurring within fuel cell systems. This knowledge will become increasingly important as energy research shifts away from the well studied PGM catalysts towards the newer non-PGM, enzyme, and microbial catalysts.

References

[1] A.D. Moodie, W.J. Ingledew, Advances in Microbial Physiology, 31 (1990) 225-268.

[2] A. Ligeza, A.N. Tikhonov, J.S. Hyde, W.K. Subczynski, Biochim. Biophys. Acta, 1365 (1998) 453-463.

[3] R. Boulatov, Billion-Year-Old Oxygen Cathode that Actually Works: Respiratory Oxygen Reduction and its Biomimetic Analogs, in: J.H. Zagal, F. Bedioui, J.P. Dodelet (Eds.) N_4-Macrocyclic Metal Complexes, Springer Science+Business Media, Inc., New York, 2006, pp. 1-40.

[4] S. Ferguson-Miller, G.T. Babcock, Chem. Rev., 96 (1996) 2889-2907.

[5] M.M. Pereira, M. Santana, M. Teixeira, Biochim. Biophys. Acta, 1505 (2001) 185-208 and references therein.

[6] R.L. Arechederra, S.D. Minteer, Fuel Cells, 9 (2009) 63-69.

[7] R.L. Arechederra, S.D. Minteer, Electrochim. Acta, doi: DOI: 10.1016/j.electacta.2009.09.083 (2009).

[8] R.L. Arechederra, B.L. Treu, S.D. Minteer, J. Power Sources, 173 (2007) 156-161.

[9] C.M. Halliwell, E. Simon, C.S. Toh, A.E.G. Cass, P.N. Bartlett, Bioelectrochemistry, 55 (2002) 21-23.

[10] M.N. Germain, R.L. Arechederra, S.D. Minteer, J. Am. Chem. Soc., 130 (2008) 15272.

[11] G.T.R. Palmore, H. Bertschy, S.H. Bergens, G.M. Whitesides, J. Electroanal. Chem., 443 (1998) 155-161.

[12] S.C. Barton, H.H. Kim, G. Binyamin, Y.C. Zhang, A. Heller, J. Phys. Chem. B, 105 (2001) 11917-11921.

[13] A. Heller, Curr. Opin. Chem. Biol., 10 (2006) 664-672.

[14] N. Mano, F. Mao, A. Heller, J. Am. Chem. Soc., 125 (2003) 6588-6594.

[15] V. Soukharev, N. Mano, A. Heller, J. Am. Chem. Soc., 126 (2004) 8368-8369.

[16] I. Willner, V. Heleg-Shabtai, R. Blonder, E. Katz, G.L. Tao, A.F. Buckmann, A. Heller, J. Am. Chem. Soc., 118 (1996) 10321-10322.

[17] G. Yildiz, F. Kadirgan, J. Electrochem. Soc., 141 (1994) 725-730.

References

[18] A. Kahyaoglu, B. Beden, C. Lamy, Electrochim. Acta, 29 (1984) 1489-1492.

[19] A. Heller, PCCP, 6 (2004) 209-216.

[20] E. Katz, I. Willner, A.B. Kotlyar, J. Electroanal. Chem., 479 (1999) 64-68.

[21] D. Sokic-Lazic, S.D. Minteer, Electrochemical and Solid State Letters, 12 (2009) F26-F28.

[22] P.A. Srere, Trends Biochem. Sci, 10 (1985) 109-110.

[23] J. Ovadi, P.A. Srere, International Review of Cytology - a Survey of Cell Biology, Vol 192, 192 (2000) 255-280.

[24] P.A. Srere, Annual Review of Biochemistry, 56 (1987) 89-124.

[25] L. Marcinkeviciene, I. Bachmatova, R. Semenaite, R. Rudomanskis, G. Brazenas, R. Meskiene, R. Meskys, Biotechnol. Lett, 21 (1999) 187-192.

[26] M. Ameyama, Methods Enzymol., 89 (1982) 20-29.

[27] M. Trinei, J.-P. Vannier, M. Beurton-Aimar, V. Norris, Mol. Microbiol., 53 (2004) 41-53.

[28] K. Jorgensen, A.V. Rasmussen, M. Morant, A.H. Nielsen, N. Bjarnholt, M. Zagrobelny, S. Bak, B.L. Moller, Current Opinion in Plant Biology, 8 (2005) 280-291.

[29] L. Yunfeng, A novel protein delivery platform based on single protein nano capsules, in: Biomedical Engineering Seminar, University of New Mexico, 2010.

[30] M.J. Moehlenbrock, T.K. Toby, A. Waheed, S.D. Minteer, J. Am. Chem. Soc., 132 (2010) 6288-6289.

[31] Glucose Oxidase Assay Procedure, in, Megazyme International 2011, pp. 1-7.

[32] T. Mueller, Biomimetics: Design by Nature, in: National Geographic, 2008.

[33] B. García-Alvarez, R. Melero, F.M.V. Dias, J.A.M. Prates, C.M.G.A. Fontes, S.P. Smith, M.J. Romão, A.L. Carvalho, O. Llorca, J. Mol. Biol., 407 (2011) 571-580.

[34] C. Fontes, H.J. Gilbert, Cellulosomes: Highly Efficient Nanomachines Designed to Designed to Deconstruct Plant Cell Wall Complex Carbohydrates, in: Annual Review of Biochemistry, Vol 79, vol. 79, Annual Reviews, Palo Alto, 2010, pp. 655-681.

[35] O. Alber, B. Dassa, E. Bayer, Cellulosome, in: E. Bayer (Ed.) CAZypedia 2010.

[36] F. Sabathé, P. Soucaille, J. Bacteriol., 185 (2003) 1093-1096.

[37] C. Teller, I. Willner, Trends Biotechnol., 28 (2010) 619-628.

[38] J. Müller, C.M. Niemeyer, Biochem. Biophys. Res. Commun., 377 (2008) 62-67.

[39] S. Ranganathan, N. Jayaraman, D. Chatterji, Biopolymers, 41 (1997) 407-418.

[40] M. Papworth, P. Kolasinska, M. Minczuk, Gene, 366 (2006) 27-38.

[41] G.T.R. Palmore, Trends Biotechnol., 22 (2004) 160-160.

[42] F. Barriere, P. Kavanagh, D. Leech, Electrochim. Acta, 51 (2006) 5187-5192.

[43] R. Sahney, S. Anand, B.K. Puri, A.K. Srivastava, Anal. Chim. Acta, 578 (2006) 156-161.

[44] J.N. Patel, B. Gray, B. Kaminska, B. Gates, Electrical and Computer Engineering, (2007) 421-424.

[45] R.L. Arechederra, K. Boehm, S.D. Minteer, Electrochim. Acta, 54 (2009) 7268-7273.

[46] BI 2000 SPR Instrument Installation and Training Tutorial, in: BI 2000 SPR Instrument, Biosensing Instruments.

[47] F. Lisdat, R. Dronov, H. Mohwald, F.W. Scheller, D.G. Kurth, Chem. Commun., (2009) 274-283.

[48] C.I. Stains, J.R. Porter, A.T. Ooi, D.J. Segal, I. Ghosh, J. Am. Chem. Soc., 127 (2005) 10782-10783.

[49] J.A. Schwarz, C.I. Contescu, K. Putyera, Carbon Nanotubes for Storage of Energy: Super Capacitors, in: Dekker Encyclopedia of Nanoscience and Nanotechnology, Marcel Dekker, Inc., 2004, pp. 540-544.

[50] S. Shleev, M. Pita, A.I. Yaropolov, T. Ruzgas, L. Gorton, Electroanal., 18 (2006) 1901-1908.

[51] A.J. Bard, L.R. Faulkner, Electrochemical Methods Fundamentals and Applications, 2 ed., John Wiley & Sons, Inc., Hoboken, NJ, 2001.

[52] Pine Research Instrumentation E7 Series ThinGap RRDEs Dimensions, in, Raleigh, NC, 2011, pp. Pine Research Instrumentation E7 Series ThinGap RRDEs Dimensions.

[53] S. Xiao, H. Zhang, C. Bi, Y. Zhang, Y. Ma, X. Li, H. Zhong, Y. Zhang, J. Power Sources, 195 (2010) 8000-8005.

[54] S.L. Gojkovic, S. Gupta, R.F. Savinell, Electrochimica Acta, 45 (1999) 889-897.

[55] K.L. Hsueh, D.T. Chin, S. Srinivasan, J. Electroanal. Chem., 153 (1983) 79-95.

[56] C.M.A. Brett, A.M.O. Brett, Electrochemistry Principles, Methods, and Applications, Oxford University Press Inc., New York, NY, 1993.

[57] N. Anastasijevic, Z.M. Dimitrijevic, R.R. Adzic, Electrochim. Acta, 37 (1992) 457-464.

[58] M.C. Machczynski, E. Vijgenboom, B. Samyn, G.W. Canters, Protein Sci., 13 (2004) 2388-2397.

[59] SDS-gel electrophoresis, in, Molecular Station, 2012.

[60] M. ElrodErickson, M.A. Rould, L. Nekludova, C.O. Pabo, Structure, 4 (1996) 1171-1180.

[61] I.R. Wheeldon, S.C. Barton, S. Banta, Biomacromolecules, 8 (2007) 2990-2994.

[62] I.R. Wheeldon, E. Campbell, S. Banta, J. Mol. Biol., 392 (2009) 129-142.

[63] S. Banta, I.R. Wheeldon, M. Blenner, Annual Review of Biomedical Engineering, Vol 12, 12 (2010) 167-186.

[64] I.R. Wheeldon, J.W. Gallaway, S.C. Barton, S. Banta, Proc. Natl. Acad. Sci. USA, 105 (2008) 15275-15280.

[65] M. ElrodErickson, T.E. Benson, C.O. Pabo, Structure, 6 (1998) 451-461.

[66] J. Gallaway, I. Wheeldon, R. Rincon, P. Atanassov, S. Banta, S.C. Barton, Biosensors & Bioelectronics, 23 (2008) 1229-1235.

[67] E.I. Solomon, U.M. Sundaram, T.E. Machonkin, Chem. Rev., 96 (1996) 2563-2605.

[68] O. Farver, A.W.J.W. Tepper, S. Wherland, G.W. Canters, I. Pecht, J. Am. Chem. Soc., 131 (2009) 18226-18227.

[69] T. Baas, L. Gamble, K.D. Hauch, D.G. Castner, T. Sasaki, Langmuir, 18 (2002) 4898-4902.

[70] H.A. Greisman, C.O. Pabo, Science, 275 (1997) 657-661.

[71] A. Mikolasch, F. Schauer, Appl. Microbiol. Biotechnol., 82 (2009) 605-624.

[72] F. Davis, S.P.J. Higson, Biosensors & Bioelectronics, 22 (2007) 1224-1235.

[73] D. Ivnitski, K. Artyushkova, P. Atanassov, Bioelectrochemistry, 74 (2008) 101-110.

[74] T. Reda, J. Hirst, J. Phys. Chem. B, 110 (2006) 1394-1404.

[75] G. Hong, D.M. Ivnitski, G.R. Johnson, P. Atanassov, R. Pachter, J. Am. Chem. Soc., 133 (2011) 4802-4809.

[76] T. Skalova, J. Dohnalek, L.H. Ostergaard, P.R. Osteryaard, P. Kolenko, J. Duskova, A. Stepankova, J. Hasek, J. Mol. Biol., 385 (2009) 1165-1178.

[77] M.J. Gorman, N.T. Dittmer, J.L. Marshall, M.R. Kanost, Insect Biochem. Molec., 38 (2008) 817-824.

[78] M.F. Hullo, I. Moszer, A. Danchin, I. Martin-Verstraete, J. Bacteriol., 183 (2001) 5426-5430.

[79] A.M. Mayer, R.C. Staples, Phytochemistry, 60 (2002) 551-565.

[80] S.C. Barton, J. Gallaway, P. Atanassov, Chem. Rev., 104 (2004) 4867-4886.

[81] E.I. Solomon, J. Inorg. Biochem., 47 (1992) 29.

[82] E.I. Solomon, R.K. Szilagyi, S.D. George, L. Basumallick, Chem. Rev., 104 (2004) 419-458.

[83] K. Piontek, M. Antorini, T. Choinowski, J. Biol. Chem., 277 (2002) 37663-37669.

[84] J. Yoon, B.D. Liboiron, R. Sarangi, K.O. Hodgson, B. Hedman, E.I. Solomona, Proc. Natl. Acad. Sci. USA, 104 (2007) 13609-13614.

[85] L. Rulisek, E.I. Solomon, U. Ryde, Inorg. Chem., 44 (2005) 5612-5628.

[86] D.B. Rorabacher, Chem. Rev., 104 (2004) 651-697.

[87] S.K. Lee, S.D. George, W.E. Antholine, B. Hedman, K.O. Hodgson, E.I. Solomon, J. Am. Chem. Soc., 124 (2002) 6180-6193.

[88] D. Ivnitski, P. Atanassov, Electroanal., 19 (2007) 2307-2313.

[89] P. Giardina, V. Faraco, C. Pezzella, A. Piscitelli, S. Vanhulle, G. Sannia, Cell Mol. Life Sci., 67 (2010) 369-385.

[90] A.A. Gewirth, M.S. Thorum, Inorg. Chem., 49 (2010) 3557-3566.

[91] G. Gupta, C. Lau, V. Rajendran, F. Colon, B. Branch, D. Ivnitski, P. Atanassov, Electrochem. Commun., 13 (2011) 247-249.

[92] O. Einarsdóttir, M.G. Choc, S. Weldon, W.S. Caughey, J. Biol. Chem., 263 (1988) 13641-13654.

[93] N. Watanabe, M.A.V. Devanathan, J. Electrochem. Soc., 111 (1964) 615-619.

[94] G.V. Shteinberg, I.A. Kukushkina, Elektrochimiya, 15 (2007) 527-532.

[95] I. Bento, L.O. Martins, G.G. Lopes, M.A. Carrondo, P.F. Lindley, Dalton T., (2005) 3507-3513.

[96] C.M. Moore, N.L. Akers, A.D. Hill, Z.C. Johnson, S.D. Minteer, Biomacromolecules, 5 (2004) 1241-1247.

[97] M.J. Schrenk, R.E. Villigram, N.J. Torrence, S.J. Brancato, S.D. Minteer, J. Membr. Sci., 205 (2002) 3-10.

[98] P.K. Addo, R.L. Arechederra, S.D. Minteer, Electroanal., 22 (2010) 807-812.

[99] P.A. Jellis, S.D. Minteer, M. Patel, A. Seimiarczuk, M. Watt, R.E.K. Winter, J. Mater. Chem., 18 (2008) 2104-2111.

[100] M.J. Moehlenbrock, S.D. Minteer, Chem. Soc. Rev., 37 (2008) 1188-1196.

[101] T. Klotzbach, M. Watt, Y. Ansari, S.D. Minteer, J. Membr. Sci., 282 (2006) 276-283.

[102] D. Horton, D.R. Lineback, Method Carbohyd. Chem., 5 (1965) 403-406.

[103] E.V. Batrakova, H.Y. Han, V.Y. Alakhov, D.W. Miller, A.V. Kabanov, Pharm. Res., 15 (1998) 850-855.

[104] T.J. Thomas, K.E. Ponnusamy, N.M. Chang, K. Galmore, S.D. Minteer, J. Membr. Sci., 213 (2003) 55-66.

[105] K. Zeng, H. Tachikawa, Z.Y. Zhu, V.L. Davidson, Anal. Chem., 72 (2000) 2211-2215.

[106] N.A. Anastasijevic, V. Vesovic, R.R. Adzic, J. Electroanal. Chem., 229 (1987) 305-316.

[107] N.A. Anastasijevic, V. Vesovic, R.R. Adzic, J. Electroanal. Chem., 229 (1987) 317-325.

[108] R.P. Ramasamy, H.R. Luckarift, D.M. Ivnitski, P.B. Atanassov, G.R. Johnson, Chem. Commun., 46 (2010) 6045-6047.

[109] S. Tsujimura, K. Kano, T. Ikeda, J. Electroanal. Chem., 576 (2005) 113-120.

[110] E.V. Batrakova, H.Y. Han, V.Y. Alakhov, D.W. Miller, A.V. Kabanov, Pharm. Res., 15 (1998) 850-855.

[111] S.C. Barton, Electrochim. Acta, 50 (2005) 2145-2153.

[112] A. Szabo, The Journal of Physical Chemistry, 91 (1987) 3108-3111.

[113] S.C. Barton, A.C. West, J. Electrochem. Soc., 148 (2001) A490-A495.

[114] R.F. Service, Science, 324 (2009) 1257-1259.

[115] J. Tollefson, Nature, 464 (2010) 1262-1264.

[116] L. Zhang, J.J. Zhang, D.P. Wilkinson, H.J. Wang, J. Power Sources, 156 (2006) 171-182.

[117] R. Bashyam, P. Zelenay, Nature, 443 (2006) 63-66.

[118] B.D. James, J.A. Kalinoski, K.N. Baum, Mass Production Cost Estimation for Direct H2 PEM Fuel Cell Systems for Automotive Applications: 2010 Update, in, 2010.

[119] K. Lee, L. Zhang, J. Zhang, J. Power Sources, 170 (2007) 291-296.

[120] F. Jaouen, E. Proietti, M. Lefevre, R. Chenitz, J.-P. Dodelet, G. Wu, H.T. Chung, C.M. Johnston, P. Zelenay, Energy & Environmental Science, 4 (2011) 114-130.

[121] M. Lefevre, J.P. Dodelet, P. Bertrand, J. Phys. Chem. B, 106 (2002) 8705-8713.

[122] F. Jaouen, M. Lefevre, J.P. Dodelet, M. Cai, J. Phys. Chem. B, 110 (2006) 5553-5558.

[123] B. Wang, J. Power Sources, 152 (2005) 1-15.

[124] C.W.B. Bezerra, L. Zhang, K. Lee, H. Liu, A.L.B. Marques, E.P. Marques, H. Wang, J. Zhang, Electrochim. Acta, 53 (2008) 4937-4951.

[125] N. Ramaswamy, S. Mukerjee, Advances in Physical Chemistry, 2012 (2012) 17.